Consistent Controls on Trace Metal Micronutrient Speciation in Wetland Soils and Stream Sediments

Jinshu Yan[1], Neha Sharma[2], Elaine D. Flynn[1], Daniel E. Giammar[2], Grace E. Schwartz[3†], Scott C. Brooks[3], Pamela Weisenhorn[4], Kenneth M. Kemner[4], Edward J. O'Loughlin[4], Daniel I. Kaplan[5], Jeffrey G. Catalano[1*]

1. Department of Earth and Planetary Sciences, Washington University, Saint Louis, MO, 63130, USA
2. Department of Energy, Environment, and Chemical Engineering, Washington University, Saint Louis, MO, 63130, USA
3. Oak Ridge National Laboratory, Oak Ridge, TN, 37830, USA
4. Argonne National Laboratory, Lemont, IL, 60439, USA
5. Savannah River National Laboratory, Aiken, SC, 29808, USA

*Corresponding author: catalano@wustl.edu
[†]Present address: Department of Chemistry, Wofford College, Spartanburg, SC 29303, USA

Submitted to *Geochimica et Cosmochimica Acta*

ABSTRACT

Trace metal are essential for microbially-mediated biogeochemical processes occurring in anoxic wetland soils and stream bed sediments, but low availability of these elements may inhibit anaerobic element cycling and transformations. Solid-phase speciation is likely a critical control on trace metal availability but has seen limited study in anoxic systems having concentrations similar to geological background levels, where metal limitations may be most prevalent. We have investigated trace metal concentrations and solid-phase speciation in three freshwater subsurface aquatic systems: marsh wetland soils, riparian wetland soils, and the sediments of a streambed. These systems displayed low solid-phase trace metal concentrations, generally at or below geological background levels, which generally followed the trend Zn > Cu ≈ Ni > Co and showed no correlation with major element compositions. All soils and sediments were dominated by quartz but varied in clay mineralogy as well as the organic matter, total sulfur, and total iron contents. X-ray absorption near-edge structure (XANES) spectroscopy shows that sulfur speciation in both wetlands is dominated by organic sulfur. Elemental sulfur and iron sulfides together made up <25% of the sulfur in the wetland soils, but the distribution between inorganic and organic forms was reversed in the stream sediments. Ferrous and ferric iron in clay minerals were common species identified by both XANES and extended X-ray absorption fine structure (EXAFS) spectroscopies at all sites. Iron(III) oxides were substantial components in all but the marsh wetland soils. Quantitative analysis of copper, nickel, and zinc XANES spectra revealed similar metal speciation across all sites. Copper speciation was dominated by sulfides, adsorbed species, and minor amounts of copper bound to organic matter; no metallic copper was detected. Nickel speciation also varied little and was dominated by nickel in clay mineral octahedral sheets and nickel sulfide, with adsorbed species also present. Zinc speciation was slightly more varied, with

68 the marsh wetland soils and stream bed sediments containing adsorbed species, zinc associated
69 with clay mineral structures, and zinc bound to reduced sulfur groups on organic matter, whereas
70 the riparian wetland soils lacked clay-associated zinc but contained zinc sulfide. Trace metals
71 bound to reduced sulfur occurred at every site, with a greater sulfur-bound fraction for copper. The
72 fractional abundance of sulfur-bound species showed no relationship with soil or sediment total
73 sulfur content, which varied by two orders of magnitude. More broadly, the observations in this
74 study suggest that trace metal speciation in freshwater wetland soils and stream sediments is
75 consistently dominated by a small set of recurring components which are distinct for each metal.
76 This may represent a general geochemical phenomenon in anoxic soils and sediments containing
77 trace metals at background concentrations (as low as 3 $\mu g\ g^{-1}$) that was not predicted from systems
78 that are contaminated with or naturally-enriched in copper, nickel, or zinc.
79

1. INTRODUCTION

Subsurface aquatic systems in freshwater environments, such as wetland soils and stream sediments, are foci of diverse anaerobic biogeochemical processes (Bowden, 1987; McClain et al., 2003; Kocar and Fendorf, 2009; Zarnetske et al., 2011; Arora et al., 2016; Neumann et al., 2016). Denitrification and methanogenesis in freshwater aquatic systems serve as important sources to the atmosphere of the greenhouses gases N_2O and CH_4, respectively (Groffman et al., 1998; Glatzel et al., 2008; Bouwman et al., 2013; Kirschke et al., 2013; Tian et al., 2015; Zhang et al., 2017). Substantial mercury methylation and subsequent emission also occur in these settings (St Louis et al., 1994; Skyllberg, 2008; Schaefer et al., 2014; Riscassi et al., 2016; Singer et al., 2016; Yang et al., 2016). Many of these processes in subsurface aquatic systems also couple to the biogeochemical cycling of other elements, such as iron and sulfur (Koretsky et al., 2003; Hlaváčová et al., 2005; Hansel et al., 2015; Segarra et al., 2015; Glodowska et al., 2020).

While the biogeochemistry of aquatic systems has been widely studied from the perspective of redox conditions, substrate availability, and thermodynamic controls on metabolic processes (Falkowski et al., 1998; LaRowe and Van Cappellen, 2011; Flynn et al., 2014; Arora et al., 2016; Danczak et al., 2016; Janot et al., 2016), there is a growing recognition of the importance of trace metal availability in affecting biogeochemical processes (Basiliko and Yavitt, 2001; Glass and Orphan, 2012; Jacquot et al., 2014). Elements that include cobalt, nickel, copper, and zinc serve as key reaction centers in metalloenzymes (Gärtner et al., 1993; Ermler et al., 1997; Thauer, 1998; Brown et al., 2000; Parks et al., 2013; Zheng et al., 2016) and their low availability has been documented in laboratory studies to inhibit methanogenesis, nitrous oxide reduction to nitrogen, and mercury methylation (Schönheit et al., 1979; Granger and Ward, 2003; Ekstrom and Morel, 2008; Glass and Orphan, 2012; Lu et al., 2018). The geochemistry of trace metals in aquatic

systems may thus have a direct impact on biogeochemical cycling of carbon, nutrients, and contaminants.

The availability of trace metals in wetland soils and stream sediments is expected to be controlled by their chemical speciation rather than bulk concentration (Worms et al., 2006; Harmsen, 2007; Zhao et al., 2016). Past studies have identified an array of chemical forms of trace metals in similar types of anoxic settings, although these have often focused on locations containing elevated metal concentrations because of environmental contamination or geogenic enrichments. Of the trace metals, copper is the most widely studied in anoxic subsurface aquatic systems. Copper sulfides and metallic copper are generated in contaminated soils, often in nanoparticulate form, upon flooding (Weber et al., 2009a; Weber et al., 2009b; Fulda et al., 2013a; Hofacker et al., 2013b; Xia et al., 2018; Cervi et al., 2021), with organic matter then potentially stabilizing these phases under oxic conditions (Fulda et al., 2013b; Mantha et al., 2019). Copper sulfides were also observed in contaminated paddy soils (Yang et al., 2015; Sun et al., 2016) and a copper-rich bog (Lett and Fletcher, 1980). Binding to organic matter, including as Cu(I) species, may be important in contaminated, flooded soils with limited sulfate (Fulda et al., 2013a; Fulda et al., 2013b). A recent study examined uncontaminated transitional and anoxic soils and found copper binds extensively to organic matter but also forms copper sulfide and minor metallic copper in the anoxic zone (Mehlhorn et al., 2018).

Fewer studies have examined the speciation of other essential trace metals in subsurface aquatic systems. In diverse coastal sediments that drain ultramafic laterite deposits highly elevated in nickel, this metal occurs coprecipitated with iron sulfides and in the octahedral sheets of clay minerals (Noël et al., 2015; Noël et al., 2017; Merrot et al., 2019). While nickel speciation in other anoxic systems has seen limited study, contaminated or enriched oxic soils contain nickel in

phyllosilicate and iron oxide structures, associated with gibbsite phases in clay interlayers, and bound to organic matter (Manceau et al., 2005; McNear et al., 2007; Dublet et al., 2012; Siebecker et al., 2017; Siebecker et al., 2018). Zinc sulfide forms under anoxic conditions in metalliferous peatlands (Yoon et al., 2012), contaminated lake sediments (Webb and Gaillard, 2015), and in a contaminated wetland, along with zinc carbonate, adsorbed zinc, and possibly zinc oxide (Bostick et al., 2001). Similar to nickel, exploration of zinc in other anoxic soil systems is generally lacking, but in contaminated oxic soils zinc sulfide, zinc in phyllosilicate octahedral sheets, and adsorbed species are common (Manceau et al., 2004; Voegelin et al., 2005; Jacquat et al., 2009; Voegelin et al., 2011; Williams et al., 2011). Less is known regarding cobalt speciation because of the difficulty probing this element using available methods in the presence of iron. Binding studies suggest that adsorbed species and complexes with organic matter are important in aerobic soils (Woodward et al., 2018) and that cobalt readily incorporates into pyrite under anoxic conditions (Swanner et al., 2019).

Prior studies provide important insight into trace metal species in anoxic subsurface systems that are contaminated with or naturally elevated in metals. All metals show occurrence as sulfide phases, although some results, such as nickel associating with pyrite in coastal sediments, may not be transferable to freshwater systems that are generally low in sulfur (Brown, 1985; Wieder et al., 1985; Spratt and Morgan, 1990; Prietzel et al., 2009). Similarly, nickel and zinc often occur in clay structures, likely produced through a neoformation process (Manceau et al., 1999; Ford and Sparks, 2000; Schlegel et al., 2001; Dähn et al., 2002), but it is unclear whether such species form when metals are not elevated in concentration from contamination or natural enrichment. The solid-phase trace metal concentrations in most prior studies of metal speciation in subsurface aquatic systems (Lett and Fletcher, 1980; Bostick et al., 2001; Weber et al., 2006;

149 Weber et al., 2009b; Weber et al., 2009a; Yoon et al., 2012; Fulda et al., 2013b; Fulda et al., 2013a;
150 Hofacker et al., 2015; Noël et al., 2015; Yang et al., 2015; Sun et al., 2016; Noël et al., 2017; Xia
151 et al., 2018; Mantha et al., 2019; Merrot et al., 2019; Cervi et al., 2021) far exceed geological
152 background levels (Rudnick and Gao, 2003): 280 to 23000 ug g^{-1} Cu versus 28±4 ug g^{-1}
153 background, 255 to 6044 ug g^{-1} Ni versus 47±11 ug g^{-1} background, 1900 to 71000 ug g^{-1} Zn versus
154 67±6 ug g^{-1} background. Investigations of speciation in wetland soils and stream sediments with
155 metal concentrations similar to geological background levels are rare (Webb and Gaillard, 2015;
156 Mehlhorn et al., 2018). However, such metal concentrations are widespread in nature (Caritat et
157 al., 2018) and likely representative of the large majority of freshwater wetlands and streambeds
158 where biogeochemical carbon, nitrogen, and mercury cycling occur in terrestrial ecosystems.
159 Anoxic subsurface systems displaying background metal levels should more frequently exhibit
160 metal limitations on biogeochemical processes than contaminated or naturally-enriched systems
161 However, the dominant controls on metal speciation in environments with low metal contents are
162 unclear. A central challenge to investigating metal speciation in relevant anoxic subsurface
163 systems is the difficulty in applying X-ray spectroscopic techniques to soils and sediments having
164 low (<100 ug g^{-1}) element concentrations.

165 In this work, we assess the variability in trace metal speciation in the subsurface of diverse
166 freshwater aquatic systems. Three field sites are investigated that are distributed over a ~1000 km
167 transect, each occurring in geologically-distinct regions representing different types of subsurface
168 aquatic system: marsh wetland soils, riparian wetland soils, and stream bed sediments. Duplicate
169 soil or sediment cores and overlying surface waters were collected in two locations at each of the
170 three study areas. Major element and trace metal concentrations, dissolved and extractable
171 nutrients, and soil and sediment mineralogy were evaluated at these sites. X-ray absorption

spectroscopy evaluated bulk sulfur and iron speciation and quantified the solid-phase speciation of nickel, copper, and zinc. The latter measurements overcame the low concentrations of trace metals by utilizing a synchrotron beamline configuration optimized for high-sensitivity measurements. Metal speciation was compared across sites to identify the dominant forms of trace metals occurring in subsurface aquatic systems.

2. MATERIALS AND METHODS

2.1 Study Sites Descriptions

Three field sites (Fig. S1) were investigated to explore diverse wetland and stream settings, each of which has been previously studied in other contexts (Van Lonkhuyzen and LaGory, 1994; Van Lonkhuyzen et al., 2004; Southworth et al., 2013; Donovan et al., 2014; Riscassi et al., 2016; Flynn et al., 2017; Schwartz et al., 2019; Kaplan et al., 2020). At each site, two locations were studied to examine the variability in metal speciation in similar settings. Marsh wetlands at Argonne National Laboratory (ANL) in Lemont, Illinois, U.S.A. were sampled in October 2018. Sampling location "Marsh 1" (41°42'19.69"N 87°59'55.04"W WGS 84) is an ~1800 m^2 marsh surrounded by deciduous forest. It contained shallow surface water at the time of sampling but becomes unsaturated during prolonged dry periods. Location "Marsh 2" (41°42'6.78"N 87°59'39.66"W WGS 84) consists of a ~3700 m^2 marsh containing open water in the center surrounded by an ~15 m vegetated border; this site maintains water saturation throughout most years. Sampling locations Marsh 1 and 2 have internal designations as wetlands 401 and 405 at ANL (Van Lonkhuyzen and LaGory, 1994).

Sediments and surface waters were sampled at East Fork Poplar Creek (EFPC) in Oak Ridge, Tennessee, U.S.A. in October 2018. Sampling locations "Stream 1" (35°57'57.89"N

84°21’32.81”W WGS 84) and “Stream 2” (36°00’06.13”N 84°14’55.10”W WGS 84) are located approximately 15 km apart. Location Stream 1 is 5.4 km upstream of the mouth of the creek, and Stream 2 is in a broader stretch 22 to 23 km upstream from the mouth. Sediments were collected from the northwest or north stream bank for locations Stream 1 and Stream 2, respectively. Sampling occurred 25 days after the last significant rain event (rain >12 mm). EFPC is impacted by point source contamination with mercury, but not other metals, originating at its headwaters (Brooks and Southworth, 2011) and receives discharge from a wastewater treatment plant about midway between the two sampling locations.

The third study site is a riparian wetland in the Tims Branch (TB) watershed at the Savannah River Site in Aiken County, South Carolina, U.S.A. Samples were collected in February 2019 at two locations, “Riparian 1” (33°20'15.36"N 81°43'5.88"W WGS 84) and “Riparian 2” (33°20'9.24"N 81°43'8.04"W WGS 84). These differed in their apparent local hydrology, with Riparian 2 showing evidence of shallow groundwater inputs at the time of sampling, which was not observed at the other location. This forested site varies in its water inundation throughout the year and in summer may lack surface water for short periods of time. Note that a section of the Tims Branch watershed 1 to 2 km downstream of the sampling locations received historical discharge of drainage waters containing metals, including uranium (Kaplan et al., 2020). This discharge was introduced through a tributary and did not impact the study areas.

2.2. Soil and Water Sampling

At each sampling site, surface water samples were collected prior to soil or sediment coring. Subsamples of the surface waters were filtered using 0.22 μm mixed cellulose ester (MCE) syringe filters. A portion of the filtered water was acidified to 2% nitric acid (HNO_3) in the field

using concentrated trace metal grade HNO_3 for dissolved major elements and trace metal analysis. The rest of the filtered water was stored on ice and immediately divided and frozen or stored at 4° C upon return to the laboratory for nutrient and anion analysis, respectively. Field process blanks were prepared using ultrapure water (>18.2 MΩ cm) following the same procedures as the surface water samples to monitor possible metal contamination during the sampling. The pH, temperature, and conductivity of the surface waters were also measured during sampling at the marsh wetlands and stream sites using a Hanna Instruments HI98194 multiparameter meter. A meter malfunction prevented data collection at the riparian wetlands; temperature and pH data for these sampling locations are taken from measurements made in January 2019, a few weeks prior to soil and water sample collection. Measurements of pH made in August 2020 at the same sampling locations in the riparian wetlands were within 0.03 pH units of those measured in January 2019, suggesting that the pH values are temporally stable at these sites.

Duplicate soil and sediment samples from each of the two studied locations at the marsh wetland and stream sites were collected by hand-coring using 7.6 cm diameter acid-cleaned polycarbonate tubes, which were then capped and sealed in the field. Cores from the marsh site were placed in a cooler on ice and transported to Washington University, where they were extruded within six hours of sampling and then transferred to an anaerobic chamber (Coy Laboratory Products, 3% H_2/97% N_2 with Pd catalyst). Cores from the stream site were extruded within one hour of sampling in a laboratory at Oak Ridge National Laboratory, transferred to an anaerobic chamber, and then impulse sealed in polyethylene pouches. An inner pouch contained each extruded sample, and this was then sealed in an outer pouch. The gas headspace in both pouches were that of the anaerobic chamber and an oxygen scavenging sachet (BD GasPak™ EZ Anaerobic Container System Sachets with Indicator) was placed in the outer pouch to minimize the risk of

leakage causing oxidation. These doubly-contained samples were removed from the anaerobic chamber after sealing, stored at 4°C, and then transported on ice to Washington University, where they were immediately transferred to an anaerobic chamber. Duplicate soil samples from each of the two study locations at the riparian wetland site were collected using 2.5 cm diameter polycarbonate tubes. These were sealed in the field, stored overnight at 4°C, and then shipped overnight to Washington University packaged with reusable ice packs, where they were then extruded and transferred to an anaerobic chamber. All cores were divided during extrusion based on visual changes in properties (e.g., soil horizons) when apparent or to divide the core length into two equal sections, with the resulting surface layer comprising the upper 4.5 to 9 cm (Table 1). All cores were segmented into two sections except for the second core from location Stream 2, which was longer and thus divided into three segments. For naming purposes, the core segments of each type were labeled using the convention CX-Y, with X being 1 or 2 to distinguish the duplicate cores and Y being 1, 2, or 3 (only for core 2 from location Stream 2) to indicate the segment starting with a value of 1 for the surface layer.

2.3 Surface Water Characterization

The field acidified surface water samples were used to determine dissolved major elements (sodium, magnesium, aluminum, silicon, potassium, calcium) using a Thermo Scientific iCap 7400 Duo inductively-coupled plasma optical emission spectrometer (ICP-OES). Dissolved trace metal (cobalt, nickel, copper, and zinc), iron, and manganese concentrations were determined by inductively-coupled plasma mass spectrometry (ICP-MS) using a PerkinElmer Elan DRC II instrument. Dissolved anions (Br^-, Cl^-, F^-, and SO_4^{2-}) in the unacidified, filtered water samples were measured using a Thermo Scientific Dionex Integrion High Pressure Ion Chromatograph (IC)

using a conductivity detector. The anion concentrations were determined using a Dionex IonPac™ AS19 analytical column (4×250 mm) and Dionex IonPac™ AG19 guard column (4×50 mm) set to 30°C with the eluent generated from a Dionex eluent generator cartridge (EGC 500 KOH). The eluent concentration was set to 10 mM KOH for 10 minutes then gradually increased to 45 mM KOH over 15 minutes before holding steady at 45 mM KOH for 5 minutes. The flow rate remained constant at 1 mL min^{-1}. Dissolved nitrate, ammonium, and orthophosphate were measured spectrophotometrically on a Seal Analytical AQ300 Discrete Multi-Chemistry Analyzer using frozen, field-filtered surface water samples that were thawed overnight at 4°C before analysis. Reagents and calibration standards were prepared using reagent grade chemicals. Ammonia was measured by reaction of a sample with hypochlorite in an alkaline solution, which is subsequently reacted with phenol in the presence of nitroferricyanide, with absorbance of the resulting blue indophenol dye measured at 660 nm. Nitrate was analyzed by reduction to nitrite by cadmium which then reacts with sulfanilamide in dilute phosphoric acid and binds to N-(1-napthyl)-ethylenediamine dihydrochloride, with the resulting azo dye detected at 520 nm. Phosphate analysis involves the reaction of samples with ammonium molybdate and potassium antimonyl tartrate in in dilute sulfuric acid, forming a complex that is then reduced by ascorbic acid, with the resulting colored complex quantified at 660 nm. Charge balance calculations and estimation of dissolved CO_2 concentrations were performed in the React module of The Geochemist's Workbench® (Bethke, 2007) version 12.0.6 using the Lawrence Livermore National Laboratory thermochemical database V8 R6 (Delaney and Lundeen, 1990). Although not measured during initial analyses because of an oversight, dissolved inorganic carbon (DIC) and dissolved organic carbon (DOC) were measured in May 2021 using a Shimadzu TOC-L total organic carbon analyzer for archived filtered (0.45 μm MCE) water samples that had been stored at 4°C.

287

288 **2.4 Solid Phase Characterization**

289 Soil and sediment core segments were mechanically mixed in the anaerobic chamber to
290 homogenize the materials prior to analysis. Approximately 20 g of wet sediment from each core
291 segment were dried in a convection oven at 40 ℃ for determining the moisture content of the soils
292 and sediments and for further bulk analyses. Sediments were then ground with a pestle and mortar
293 and stored in glass vials. 1 g of each sediment sample was micronized in isopropanol using a
294 McCrone Micronizing Mill to obtain a fine powder. The fine powders were then analyzed by
295 powder X-ray diffraction (XRD) on a Bruker d8 Advance diffractometer using Cu Kα radiation
296 (40 kV, 40 mA) and a LynxEye XE energy-dispersive silicon-strip detector. XRD patterns of all
297 sediment segments were performed from 3° to 80° 2θ with a 0.02° 2θ step-size, a collection time
298 of 1.0 s per step, and no sample rotation to enable measurement to low angle. The detector consists
299 of 192 independent strips, each of which measured each 2θ position for the 1.0 s collection time,
300 yielding a net integration time of 192 s per data point. The Bruker Diffrac.Eva application was
301 used for phase identification using patterns generated from crystal structures contained in the
302 Crystallography Open Database (Graulis et al., 2009).

303 Total nitrogen, carbon, and sulfur contents were determined using these dried soil and
304 sediment samples by combustion elemental analysis using an Elementar vario MACRO cube
305 CHNS analyzer. Approximately 0.1 to 0.2 g of the dried, ground soils or sediments from all core
306 segments were measured in triplicate. The total metal concentrations in the soils and sediments
307 were estimated using a microwave digestion analysis method (Hassan et al., 2007). Specifically, 3
308 mL of concentrated trace metal grade HNO_3 and 0.3 mL of 30% hydrogen peroxide (H_2O_2) were
309 added to 0.030 g of dried soil or sediment in a PTFE microwave digester vessel. Samples were

left to react at room temperature in the fume hood for 30 minutes and then digested in a CEM MARS6 microwave digestion system. The temperature was ramped from ambient to 175 °C over 10 min and then maintained at 175°C for 15 min to promote complete digestion. After the vessels cooled, samples were filtered using 0.22 µm MCE filters followed by dilution to 2% HNO_3. Triplicate digestions were prepared for each soil or sediments. Major elements (Al, Ca, Fe, K, Mg, Na, P, and S) in the resulting fluid were analyzed using ICP-OES and trace metals (Cu, Ni, Co, and Zn) plus Mn using ICP-MS.

Extractable nitrate, ammonium, and phosphate in the sediments were measured by an equilibrium extraction method adapted from previous studies (Sparks et al., 1996; Pansu and Gautheyrou, 2006). The extractions were performed in the anaerobic chamber with 1 g of moist soil or sediments suspended in 10 mL of 2 M potassium chloride (KCl). Samples were rotated end-over-end for 1 h, allowed to settle for 30 min, and then filtered using 0.22 µm MCE syringe filters. The filtrate was stored at 4 °C prior to analysis. Nitrate, ammonium, and phosphate in the extraction fluid were analyzed using a Seal Analytical AQ300. Samples from both cores at each site were treated as duplicate measurements to assess variability. The measured moisture content was used to calculate the concentration of the nutrients per gram of soil or sediment.

2.5 X-ray Absorption Spectroscopy Data Collection and Analysis

To determine the speciation of sulfur, iron, and trace metals present in the soils and sediments, X-ray absorption spectra were measured for nickel, copper, and zinc in the C1-1 segments of the cores collected at each sampling location. C2-1 from location Stream 1 was also studied because XRD identified pyrite in C1-1 but not C2-1 (see Section 3.2). Cobalt was not investigated because its signal is masked by fluorescence from iron. Samples were prepared in an

anaerobic chamber as wet pastes sealed in polycarbonate sample holders using two layers of Kapton tape backed with acrylic glue. The beam-facing side of samples prepared for sulfur analysis was sealed with Saint-Gobain CHR sulfur-free polyester tape with an acrylic backing. To preserve hydration and anoxic conditions, the sealed samples were then impulse sealed in polyethylene pouches, which also contained a cellulose fiber wiper moistened with deoxygenated ultrapure water to inhibit desiccation. Reference standards (Fig. S3-8) that required stable hydration, such as adsorbed trace metal standards, were prepared similarly. Standards that are stable as dry solids were prepared by grinding using a mortar and pestle and spreading the resulting fine powder on cellulose acetate tape. Lists of reference standards are available in Tables S7-11, including their source, synthesis procedure, or, if data were taken from the literature, the relevant citation.

Primary data collection occurred at the Stanford Synchrotron Radiation Lightsource. Nickel, copper, and zinc K-edge spectra were collected at beamline 11-2, which employs a Si (220) double crystal, variable-exit monochromator (phi = 90° orientation) to scan the incident beam energy. A Rh-coated Si collimating mirror and detuning the monochromator to ~80% of peak intensity were used to minimize the harmonic content of the X-ray beam. Nickel, copper, and zinc metal foils were used for energy calibration, with their K-edges set to 8333, 8979, and 9659 eV, respectively. Data were collected in fluorescence-yield using a 100-pixel energy-dispersive monolithic Ge detector. This large array detector captured a substantial solid-angle of the associated X-ray fluorescence emitted by each sample, maximizing the count rate originating from trace metals in the sample. Data collection focused on the X-ray absorption near-edge structure (XANES) region because of the low signal level associated with the concentrations of the trace metals. The detector was operated in a high-resolution mode to separate the fluorescence line of interest from background, which dominated the total count rate and was thus the dominant

contributor to noise in the data. Detector saturation was avoided because of the relatively low Fe content in the samples and the relative attenuation of Fe fluorescence by Al foil placed between the sample and detector. The high flux of the beamline enabled this substantial attenuation while still utilizing the full linear-range of the detector. Multiple scans were collected for each sample and then averaged. No detectable changes in the spectra were observed, such as those caused by beam-induced damage, and no drift in energy calibration was detected.

Iron and sulfur K-edge spectra were collected at beamlines 4-3 configured with a Si (111) double-crystal monochromator (phi = 90° orientation) and a Si mirror for harmonic rejection. Sulfur XANES spectra were collected in fluorescence-yield using a Vortex ME7 silicon drift detector. All samples for sulfur measurements were removed from their polyethylene pouches and immediately chilled to ~20 K using a liquid He cryostream to prevent beam-induced redox changes while minimizing beam attenuation. Iron spectra were collected through the extended X-ray absorption fine structure (EXAFS) region in transmission at ambient temperatures. Repeated scans of sulfur and iron in a single position on each sample showed negligible changes over time. However, attempts to evaluate other positions on the samples were not successful because of diffraction into the fluorescence detector and spatially heterogeneous absorption, both of which are attributed to the substantial quartz contents of the samples. Data for some standards were collected at beamlines 5-BM-D and 12-BM-B at the Advanced Photon Source at Argonne National Laboratory. These beamlines employ Si (111) fixed-offset monochromators with a flat Rh-coated Si mirror for harmonic rejection; a toroidal Rh-coated Si mirror at 12-BM-B also provides beam focusing. Data for pure compounds were collected in transmission while those with lower target element concentrations, such as elements substituting in a mineral structure, were collected in fluorescence yield using a 12-element energy-dispersive solid-state Ge detector.

XANES spectra were averaged in the Sixpack interface (Webb, 2005) to IFEFFIT (Newville, 2001) and then background subtracted and normalized in Athena (Ravel and Newville, 2005). For the trace metal spectra, E_0 was set to 8342 eV for nickel, 8988 eV for copper, and 9659 eV for zinc. These values reflect the typical edge position of the collection of samples and are thus shifted relative to the energies expected for these elements in their metallic forms. A linear pre-edge background was fitted to the pre-edge region (150 to 30 eV below E_0 for copper and nickel, and 60 to 30 eV below E_0 for zinc) and removed. The data were then normalized by fitting a linear function to the post-edge region (75 to 225 eV above E_0). For iron, E_0 was set to 7125 eV and a linear background was fitted 27 to 20 eV below E_0. This background range was narrow because some spectra had a glitch at lower energy and a consistent background removal was used for a all samples. Separate post-edge normalizations were used for the iron XANES and EXAFS spectra. For the XANES, normalization was again performed using a linear function fitted to 75 to 225 eV above E_0. To account for slight curvature in the data over the larger energy range covering the EXAFS region, the data were normalized using a quadratic function fitted between 150 and 540 eV above E_0. The EXAFS were extracted after fitting a spline using the Autobk algorithm in Athena (R_{bkg} = 0.7; *k*-weight = 3; *k*-range 3 – 11 $Å^{-1}$). The E_0 for the sulfur XANES data was set to 2472 eV, with a linear background fitted between 20 and 7 eV below E_0 and a linear post-edge normalization performed between 35 to 56 eV above E_0.

For the spectra of the trace metals, Athena was used for principal component analysis (PCA), target transformation (TT) of the spectra of standards, and linear combination fitting (LCF) of the spectra (Manceau et al., 2002). Statistical constraints on the amount of variability in a set of spectra are provided by PCA but this cannot uniquely identify the exact number of fitting components required because of limited data set size and possible co-occurrence of real species in

multiple spectra (Manceau et al., 2002). Similarly, TT provides statistical support for identifying the standards most likely to occur in a set of samples, but this is also ambiguous and needs to be guided by chemical and mineralogical constraints. Further, similar species (e.g., trace metals in clay mineral structures) may display subtle variations in their spectra that would require an impractical number of standards to fully capture. The spectrum of the actual species present in a sample may thus not be perfectly matched by that of an individual standard, but a linear mixture of two or more chemically similar standards may reproduce this well. Given these limitations and the inability to independently identify the individual trace metal species present, a combinatorial approach was used where all combinations of the spectra of relevant standards, identified by TT, were fit to the sample spectra, with the combination that minimized the reduced chi-squared value, χ_v^2 (Kelly et al., 2008) used as the final result. Fitted components were then grouped in species categories (see Section 3.4). Linear-combination fitting of sulfur XANES spectra also employed a combinatorial approach using Athena, but standards used as fitting components were selected to reproduce the features present. The spectra clearly indicated the co-occurrence of more sulfur species than there were samples, precluding use of PCA. Similarly, fitting of iron XANES and EXAFS spectra in Athena used standards based on common iron phases and mineralogy determined by XRD. We note that the insight gained from all linear combination fitting is limited by the standard spectra available. Inclusion of additional standard spectra, such as through future reuse of the data presented, may enable greater insight into the species present.

3. RESULTS

3.1. Soil and Sediment Mineralogy and Composition

The mineralogy at all sites is dominated by quartz with only minor phases showing substantial variations in occurrence (Fig. 1). The investigated duplicate core samples at each location yielded similar mineralogy (data from only one core are plotted) except at location Stream 1, with the surface layer of one of the two cores containing pyrite, the only detection of this phase (Fig. 1). Minor phases in the marsh wetland soils included smectite, illite, and kaolinite as well as plagioclase feldspar. The riparian wetland soils differ from the marsh wetland soils, with location Riparian 2 having minor K-feldspar, kaolinite, chlorite, and gibbsite, and trace illite. In contrast, the location Riparian 1 soil contains only trace amounts of kaolinite, chlorite, and gibbsite, with no other phases detected besides the ubiquitous quartz. Note that prior studies at the Savannah River Site, which hosts the riparian wetlands, suggest that clays identified by XRD as chlorite may instead be hydroxy-interlayered vermiculite (Kaplan et al., 1997; Zaunbrecher et al., 2015). The stream sediments at both sampling locations contain minor K-feldspar, chlorite, smectite, kaolinite, and illite. No carbonate minerals were detected in any sample.

The total carbon contents varied among the sites (Fig. 2), with highest concentration in the marsh soils and lesser amounts at the other two sites. Notably, the core sample containing pyrite at location Stream 1 also contained elevated organic carbon, and this was substantially lower in the pyrite-free duplicate core. It is unclear whether there is a genetic relationship between organic carbon and pyrite as the latter had sharp X-ray diffraction lines (Fig. 1), suggestive of a detrital phase. Sulfur showed a similar pattern of variation as carbon despite the substantially lower concentration. The cores at location Stream 1 showed a large difference in sulfur content, again because of the presence of pyrite in one of the two duplicates. Iron contents were similar among

all samples except for location Riparian 1, which contained an order of magnitude less iron, consistent with the mineralogy being dominated nearly exclusively by quartz. Manganese contents were two to three orders of magnitude lower than iron contents, with the lowest values observed in the riparian soils.

3.2. Trace Metal Concentrations

3.2.1. Dissolved trace metals

Dissolved trace metal concentrations (Fig. 3) generally followed the trend of Zn > Cu ≈ Ni > Co at all the investigated sites. Dissolved Zn concentrations showed the largest absolute variation, ranging from 46 to 230 nM with no clear trend among the sites, and the values were in all cases above the 10 to 20 nM concentrations in the process blanks (Table S2). Similarly, dissolved Cu concentrations showed no trend among the three field sites and ranged from 20 to 80 nM. Measured Cu concentrations were substantially greater than in the process blanks except for marsh wetland location Marsh 2. Ni concentrations were similar at the marsh wetlands and stream sites, occurring in the range of 30-60 nM, but location Riparian 2 contained substantially less dissolved Ni (12 nM). One process blank from the marsh wetland contained ~130 nM dissolved Ni while all others were <10 nM. We attribute this to contamination, possibly from dust associated with >40 km hr^{-1} wind gusts during sampling at this location. Dissolved Co concentrations were low, often <10 nM, but in most cases were above the approximately 2 to 4 nM concentrations in the process blanks.

3.2.2. Solid phase trace metals

Overall patterns of solid-phase trace metal concentrations (Fig. 3), as determined by microwave-assisted acid digestion, followed the same general trend as for the surface waters: Zn > Cu ≈ Ni > Co. Variations in the abundance of each trace metal among the field sites generally tracked one another. The marsh wetlands contained the highest solid-phase Cu, Ni, and Zn contents, with Co concentrations the largest in the stream site sediments, although this was likely affected by the presence of pyrite in one core. The riparian wetlands, especially location Riparian 2, had the lowest solid-phase trace metal contents, consistent with the low abundance of non-quartz minerals and low major element (C, S, Fe, Mn) concentrations. The concentrations of the trace metals (0.3 to 18 ug g^{-1} Co, 3 to 27 μg g^{-1} Ni, 3 to 45 μg g^{-1} Cu, and 11 to 144 μg g^{-1} Zn) were similar to or well below geological background levels of 17.3±0.6 μg g^{-1} Co, 47±11 μg g^{-1} Ni, 28±4 μg g^{-1} Cu, and 67±6 μg g^{-1} Zn (Rudnick and Gao, 2003).

3.3. Spectroscopic Analysis of Sulfur and Iron Speciation

Seven samples in total were examined from the three field sites using sulfur K-edge XANES and iron K-edge XANES and EXAFS spectroscopy. The surface layer sample from the first core at each sampling location was examined except for location Stream 1. The duplicate cores from this location differed in their mineralogy (core 1 contained pyrite) as well as their bulk carbon, iron, sulfur, and trace metal contents. Samples from both cores from location Stream 1 were thus investigated.

494 ***3.3.1. Sulfur Speciation***

495 The sulfur XANES spectra of wetland soils and stream sediments display two primary
496 whiteline regions at 2472.6 to 2474.1 eV and 2481.1 to 2482.5 eV, with some displaying a shoulder
497 near ~2470.5 eV (Fig. 4). This array of features indicate the presence of multiple sulfur oxidation
498 states occurring in both inorganic and organic forms (Prietzel et al., 2009; Manceau and Nagy,
499 2012), potentially consistent with inorganic mono- and disulfide minerals, elemental sulfur,
500 exocyclic reduced sulfur, sulfones, sulfonates, and organic or inorganic sulfates. Preliminary
501 principal component analysis (PCA) of these spectra revealed that fine-structure features were
502 present in all components. This indicates that the number of species in the samples was similar to
503 or exceeded the number of samples analyzed (seven). Further evaluation using statistical
504 techniques, including evaluation of possible standard spectra via target transform (TT), was thus
505 not possible as the sample set is inadequate to describe the variability in the data.

506 A combinatorial fitting approach was used (Manceau and Nagy, 2012) to identify the
507 species present because of the large number of species likely present. We modified the previously-
508 published procedure by using the reduced chi-squared (χ_ν^2) as the goodness-of-fit parameter to
509 minimize because it accounts for the removal of degrees of freedom when adding additional fitting
510 components. The fitting results are considered semi-quantitative because the spectra of standards
511 were taken from prior studies (Table S7) that may have differed in their energy resolutions. This
512 is most apparent for pyrite and elemental sulfur fitting components. Attempts to collect data on
513 both phases after micronizing and dispersing on sulfur-free polyester tape resulted in whitelines
514 that were lower intensity and broader than the diagnostic features in the sample spectra. This
515 indicates that the standards suffered from over-absorption, an effect that has been widely reported
516 in previous studies (George et al., 2008; Almkvist et al., 2010; Manceau and Nagy, 2012; Lau et

al., 2017). While the systematic errors associated with the standards used could not be rectified, the fitting results still constrain which sulfur species are present and their relative abundance.

Fitting demonstrates that the wetland soils and stream sediments all contain elemental sulfur, exocyclic reduced sulfur, sulfonate, and sulfate. The latter species was best modeled using inorganic sulfate, with the combinatorial fitting not identifying an organosulfate in any sample. All samples except core 2 of location Stream 1 contained a small FeS component. However, the abundance of this phase may be underrepresented in some samples as fitting did not always fully reproduce the intensity of the shoulder at ~2470.5 eV associated with the phase. Pyrite was only observed in both samples from location Stream 1. It is likely that the C1 sample measured by XANES did not contain the substantial amount of pyrite identified by XRD. Sample alignment prior to XANES data collection involves identifying an area with spatially-uniform fluorescence, and this process likely selected for areas free of coarser pyrite grains. The sharp XRD peaks indicate pyrite in the C1 samples from location Stream 1 is well crystalline, and such grains would produce locations of spatially-varying fluorescence that would be avoided during alignment. The two marsh wetland soils and the Riparian 2 sample also contained minor amounts of sulfoxides and sulfones.

3.3.2. Iron Speciation

The speciation of iron was probed using both XANES and EXAFS spectra for all sampling locations except Riparian 1 (Fig. 5). The high quartz content in this sample prevented identification of a spatially homogeneous location and all EXAFS spectra that were attempted contained substantial artifacts; only the XANES spectrum was analyzed for this sample. Preliminary PCA of the XANES and EXAFS spectra revealed fine-structure features present in all components

obtained for each spectra region. This indicates that the number of species present in the samples was equal to or greater the number of spectra measured (seven for XANES, six for EXAFS). This precluded further statistical analyses, including evaluation of potential standard spectra using TT.

Similar trends in overall speciation were observed among the samples through analysis of the XANES and EXAFS regions. However, quantitative agreement between the XANES and EXAFS fitting results did not occur for all samples. Such differences can result if the standards are more crystalline than the species present, as such cases would produce similar XANES spectra but distinct EXAFS spectra associated with weaker oscillations from more disordered second shell features in less crystalline materials. These discrepancies do not affect the overall results of this study as iron speciation was investigated primarily to constrain the potential host phases for trace metals. Any solid iron species detected would occur at two to four orders of magnitude greater abundance than the trace metals.

Iron at all sites partially occurs as Fe(II) and Fe(III) in clay mineral structures, with all but location Marsh 1 showing evidence for Fe(III) oxide minerals as well. Both core samples from location Stream 1 contained FeS, with both XANES and EXAFS showing that this phase occurs in greater abundance in core 1. No pyrite was apparent in either core from location Stream 1. Similar to the sulfur case, the need to obtain data on a portion of the sample having spatially uniform absorbance may have biased the measurement by avoiding pyrite grains. Note that the iron, sulfur, and trace metal spectra (Section 3.4.), as well as XRD patterns, were each collected on different subsamples of physically homogenized core segments because of the distinct measurement requirements. The detection of pyrite in the Stream 1 samples by sulfur XANES (Fig. 4) is thus not necessarily contradictory to the iron speciation results. We interpret these results to indicate that iron sulfide phases are present in the samples. The XANES and EXAFS spectra

are not consistent regarding FeS or pyrite occurrences in other samples. These phases have low abundances (<10 mol% of Fe) in the fitting results and may thus either be artifacts or reflect different sensitivities to minor phases. The weak shoulder at ~2470.5 in many sulfur XANES spectra is more diagnostic for a minor FeS component in many samples, suggesting this is present in small quantitates. Note that iron concentrations are an order of magnitude greater than sulfur in most samples so an ~10% FeS component in the sulfur XANES spectra would correspond to ~1% FeS in the iron spectra. Finally, most samples required a contribution from dissolved Fe(II) to reproduce the iron XANES and EXAFS spectra. This may reflect Fe(II) adsorbed to or cation exchanged onto minerals or complexed by organic matter. While no iron-bearing primary silicates were detected in XRD, we lack available XANES and EXAFS spectra for such phases, and the dissolved Fe(II) component may at least partially account for minor occurrences of such minerals. Finally, fitting of the XANES spectra identified magnetite as a minor component of only the Marsh 1 sample, and this was not observed for any EXAFS spectrum. We thus conclude that magnetite is not an observable component of the iron speciation in the sites examined.

3.4. Spectroscopic Analysis of Trace Metal Speciation

XANES spectroscopy (Fig. 6-8) was employed to investigate solid-phase trace metal speciation using the same sample selection rationale as for the sulfur and iron measurements described above. EXAFS measurements were not possible because of the low total metal contents of the samples. Cobalt was not investigated because its fluorescence signal is masked by the iron K_β fluorescence line. The resulting seven spectra per element were initially examined by PCA to evaluate variability in the XANES spectra for each element and to provide statistical guidance for the minimum number of components contained in each dataset. Target transform (TT) was then

used to assess whether the spectra of various standards for each metal (Fig. S6-8) were possibly present in each dataset. Those standard spectra which could be reconstructed by TT, minus species inconsistent with the observed mineralogy or the sulfur and iron speciation, were then used in linear-combination fitting (LCF) to quantitatively assess trace metal speciation. A combinatorial LCF approach was used, with all possible combinations of two or more standards evaluated. The fit that yielded the lowest reduced chi-squared value was then selected.

This approach was motivated by the lower sensitivity of XANES spectra to specific structural environments compared to EXAFS spectra, which are unmeasurable because of the low trace metal concentrations. In recognition of this limitation, the LCF results were binned by broad species type to more accurately reflect the information obtained. While XANES spectra reflect the general coordination environment of the target element, they lack the specific structural sensitivity of EXAFS spectra. The adsorbed metal groupings included XANES fitting contributions from the spectra of aqueous ions because these are spectrally similar to some adsorbed species (Fig. S6-8). In addition, their spectra are expected to be indistinguishable from the spectra of cation exchanged species. Dissolved species themselves are likely a negligible contribution to the spectra for all samples. Assuming maximum porewater trace metal concentrations of 1 μM, well above the dissolved concentrations in overlying surface waters (Fig. 3), aqueous species would constitute <1% of the metals per unit volume in the soil and sediment samples. The spectra of metals coordinated to carboxylic acids were also similar to the spectra of aqueous and adsorbed species and were thus binned into the adsorbed metal groupings. An analogous approach was used to establish the "clay structures" grouping, consisting of metals substituted into octahedral sheets in phyllosilicates and related phases. Clay minerals vary widely in their compositions, and the range of possible second-shell cation neighbors produces subtle variations in the fine structure features

609 of trace metal XANES spectra. There is no method available to independently determine the
610 composition of clay(s) hosting a trace metal in a sample. Sample spectra were thus fitted using the
611 spectra of a series of clay standards to account for these subtle spectral variations. All such fitting
612 components were binned into the "clay structures" grouping. The standards utilized in all analyses
613 are thus interpreted as proxies for general classes of metal species distinguishable by their local
614 coordination environments.
615
616 ***3.4.1. Copper Speciation***
617 Five of the seven copper XANES spectra (Fig. 6), spanning samples from all three sites,
618 displayed a clear shoulder at ~8986 eV indicative of copper bound to reduced sulfur. These include
619 the spectra of the duplicate core samples from location Stream 1, one of which contained pyrite.
620 Spectra from location Riparian 1 and Stream 2 displayed a weaker low-energy shoulder and
621 stronger white line. PCA required three components to adequately reconstruct the fine structure of
622 all of the sample spectra. TT identified covellite (CuS), chalcocite (Cu_2S), aqueous Cu(II), Cu(II)
623 adsorbed to goethite, copper(II) citrate, copper(II) hydroxide, and Cu(II) complexed to cysteine
624 and histidine as potential standards. While observed in prior studies (Weber et al., 2009b; Weber
625 et al., 2009a; Hofacker et al., 2013b; Hofacker et al., 2013a; Hofacker et al., 2015), metallic copper
626 was poorly reconstructed and thus unlikely to be present in the samples. Combinatorial LCF results
627 utilized all of the well-reconstructed standards in modelling the XANES spectra except for
628 copper(II) citrate, copper(II) hydroxide, and Cu(II) complexed to cysteine, which were not present
629 in any optimized fit. In the fitting results, the histidine complex is classified as representing amine-
630 bound copper, and both aqueous Cu(II) and Cu(II) adsorbed to goethite representing adsorbed
631 copper.

632 CuS was present in all sites studied and accounted for >70% of the copper in five of the
633 seven samples (Fig. 6). Adsorbed forms of copper were the next most abundant species overall,
634 present in all but location Marsh 1. This species type occurred in equal abundance as CuS at
635 location Riparian 1 and was the dominant copper species in the sediments at location Stream 2.
636 Amine-bound copper was a minor component in four samples and fitting only identified Cu_2S
637 (30±4%) at location Riparian 1. No significant difference in CuS abundance was observed for the
638 duplicate core samples from location Stream 1 despite one of these (C1) containing pyrite. While
639 fitting identified a minor amine-bound copper component in one of the two duplicate cores, its
640 occurrence is of marginal statistical significance (9±7 wt.%) and adsorbed plus amine-bound
641 copper are effectively identical for the two samples.
642
643 ***3.4.2. Nickel Speciation***
644 The nickel XANES spectra (Fig. 7) show, at most, subtle variation among all samples
645 examined. These are limited to slight variations in the slope of the absorption edge, the height and
646 shape of the white line at ~8352 eV, and the intensity of the weak post-edge feature at ~8367 eV.
647 Reconstruction of the spectra during PCA required three components to reproduce major fine-
648 structure features. A fourth component contained features consistent with XANES fine-structure
649 and further improved reconstructions of some spectra. TT identified nickel sulfide, Ni(II)
650 substituting in magnetite and the octahedral sheets of serpentine and a trioctahedral Fe(II)-Mg
651 smectite, dissolved Ni(II), Ni(II) adsorbed to goethite, and Ni(II) complexed to histidine, cysteine,
652 glutathione, and cellulose as potential standards. Of these standards, none of the organic complexes
653 occurred in the optimized fits to the data, and Ni(II) substituting in magnetite was not used because
654 magnetite was not clearly identified by XRD or the iron speciation results. For the remaining

655 standards, spectra of the Ni(II) in the octahedral sheets of serpentine and smectite were grouped as
656 “clay structures”, and Ni(II) adsorbed to goethite and in aqueous solution were grouped as
657 adsorbed Ni.

658 Fitting identified Ni in clay structures, nickel sulfide, and adsorbed Ni in all samples (Fig.
659 7). Nickel in clay mineral structures was the dominant species in all samples, ranging from 50%
660 to 70% of the total Ni. Nickel sulfide was the next most abundant species in the marsh wetlands
661 and location Stream 1, with adsorbed nickel occurring in higher abundance in the other stream site
662 and the riparian wetlands. Despite the presence of pyrite in one of the duplicate cores, the sulfide
663 component of the nickel species at stream location Stream 1 were statistically identical.

664 The quantitative nickel speciation results likely contain systematic errors associated with
665 the presence of a species not represented in the set of standards available. The spectra of a number
666 of samples, most notably the riparian wetland samples, contain a weaker feature at ~8367 eV and
667 a splitting in the broad features from 8380 to 8420 eV that are not reproduced in the fits (Fig. 7).
668 Examination of published spectra of diverse organic and mineral-associated forms of nickel
669 indicates that such features are rare in Ni K-edge XANES spectra (Kopittke et al., 2011; Van Der
670 Ent et al., 2018; Ratié et al., 2018; Siebecker et al., 2018). The 8380 to 8420 eV feature corresponds
671 to the 3 to 4 $Å^{-1}$ region of the EXAFS spectrum, and this has been shown to produce a splitting
672 when nickel occurs in Mg-rich serpentine, gibbsite (Siebecker et al., 2018), and aluminum
673 hydroxide clusters in smectite interlayers or associated with smectite as small gibbsite particles
674 (Nachtegaal et al., 2005), with the Al-modified smectites producing the deepest node in this split
675 feature. The misfit of the XANES data in the 8380 to 8420 eV region is most substantial in samples
676 containing detectable gibbsite in the XRD data, supporting the assessment that this originates from
677 nickel species associated with aluminum hydroxides. In the grouping approach used in this study,

these would be categorized as clay-associated species and thus the misfits do not fundamentally alter the observation of this group as the predominant nickel species in the samples examined. Further, the nickel sulfide content determined by the fitting is likely unaffected by the lack of an appropriate standard for this type of clay-bound nickel. Nickel sulfide has an absorption edge shifted to lower energy from all clay species and its contribution reproduces broadening of the data in the low-energy portion of the absorption edge.

3.4.3. Zinc Speciation

Similar to copper and nickel, the XANES spectra of zinc show only subtle variations except for sample Riparian 2, which lacks fine structure features in the whiteline (Fig. 8). At least three components are required to reconstruct the spectra during PCA, with four clearly improving reconstruction of features in some spectra. In addition, an examination of the individual components showed that up to five contained non-noise features. TT identified a large number of possible candidate species: zinc(II) oxide, sphalerite (ZnS), zinc(II) in the octahedral sheet of a trioctahedral Fe(II)-Mg smectite, a zinc-aluminum layered double hydroxide, zinc(II) adsorbed on and incorporated into goethite, dissolved zinc(II), zinc(II) acetate, zinc(II) oxalate, zinc(II) sulfate, and zinc(II) complexed to cysteine and glutathione. Combinatorial LCF fitting did not utilize the spectra of the layered double hydroxide, zinc oxalate, and zinc incorporated into goethite in the final results. Species were grouped by category in reporting the fitting results as described for the other metals.

Zinc speciation (Fig. 8) was similar in the marsh wetland soils and stream site sediments, consisting of adsorbed species, zinc associated with clay mineral structures, and complexed to thiol groups. The riparian wetland soils lacked Zn in clay structures and contained sphalerite, with

location Riparian 2 lacking thiol-bound zinc and location Riparian 1 containing a large adsorbed pool. In addition, a substantial zinc oxide component ranging from 10% to 54% of the zinc species occurred in all samples. Prior studies of zinc-contaminated soils have indicated that zinc oxide introduced into such settings does not persist, dissolving and transforming to new phases (Voegelin et al., 2005; Voegelin et al., 2011). An inverse correlation was observed between XANES-derived zinc oxide content and solid-phase zinc concentrations ($R = -0.81$, $p = 0.03$). These considerations suggest that the zinc oxide component may be a contaminant or data collection artifact. Notably, the cellulose acetate tape widely used for sample mounting and other purposes at synchrotron beamlines contains zinc oxide (Supplementary material text and Fig.S9). Zinc oxide introduced during field sampling is unlikely to have persisted and process blanks during microwave digestion did not identify zinc concentrations above the detection limit. The zinc oxide components in the XANES spectra are thus likely attributable to a background signal associated with sample cells and beamline components.

4. DISCUSSION

4.1 Lack of Elemental Correlations in Bulk Compositions

A linear regression employing maximum likelihood estimation and weighted by the bivariate uncertainties (Thirumalai et al., 2011) determined correlation coefficients (R) and p-values among pairs of the various major element and trace metal concentrations for each site. The datasets used in the analysis consisted of compositional data and associated measurement uncertainties for all sections of the duplicate cores from both sampling locations at each field site, e.g., cores 1 and 2 from the Marsh 1 and Marsh 2 locations at the marsh wetlands site. For the stream sediment site, the surface layer from core 1 at location Stream 1 contained pyrite and was

724 removed from the dataset because it serves as an outlier that then yields spuriously large R values.
725 In many regression analyses the pyrite-bearing sample occupied one end of a linear trend far
726 removed from all other samples, which form a separate cluster that anchors to the opposite end of
727 the linear trend. Removal of this one outlier datum in each analysis substantially changed the
728 regression line and decreased the R value.

729 Regression of trace metal and major element abundances in the marsh wetland soils and
730 stream sediments generally yield low R values (Fig. 9), indicating weak correlation among these
731 elements. No clear relationships can be identified between the trace metal and major element
732 contents of these soils and sediments. In contrast, large R values between the trace metals and all
733 major elements were obtained for the riparian wetland soils (Fig. 9), with all having high statistical
734 significance ($p \leq 0.003$). Further examination, however, shows that the major elements are also
735 highly correlated with each other, and all element pairs yield large R values with small p-values.
736 We hypothesize that the correlations among all elements (C, S, Fe, Mn, and trace metals) in the
737 riparian wetland soils reflect variations in the minor non-quartz content in which all of these
738 elements reside. Variations in major element abundance thus do not provide insight into processes
739 controlling solid-phase trace metal speciation in the soils and sediments.

740

741 **4.2. Importance of Reduced Sulfur and Clay Minerals to Background Metal Speciation**

742 ***4.2.1 Reduced Sulfur***

743 In the present study, substantial fractions of copper, nickel, and zinc in all samples were
744 bound to reduced sulfur (Fig. 10A), primarily as sulfide minerals for copper and nickel and as thiol
745 groups on organic matter for zinc. Trace metals are widely reported to associate with reduced
746 sulfur in anoxic soils and sediments in freshwater systems (Huerta-Diaz et al., 1998; Koretsky et

al., 2007), but the relationship between metal speciation and sulfur content has not been previously explored. Larger fractions of copper are associated with sulfur compared to nickel and zinc, consistent with past studies of both natural and contaminated sites (Bostick et al., 2001; Weber et al., 2009b; Fulda et al., 2013a; Noël et al., 2015; Webb and Gaillard, 2015; Siebecker et al., 2018; Mantha et al., 2019). However, no clear relationship exists between the fractions of each metal bound to reduced sulfur and the total sulfur content of the soil and sediment samples (Fig. 10B), despite nearly two orders of magnitude variation in the concentration of sulfur (Fig. 2). Prior studies suggest that metal binding to reduced sulfur in flooded soils (Weber et al., 2009b; Fulda et al., 2013a) is limited by sulfide availability. Such limitations are not apparent in the present work despite the bulk sulfur content spanning the range of concentrations in these prior investigations. This different observation may originate from the focus of prior studies on either contaminated soils with substantially higher metal concentrations or soils to which sulfate was added during anoxic incubations. At the low metal concentrations observed in the marsh and riparian wetland soils and stream sediments under examination, which are similar to crustal averages (Rudnick and Gao, 2003), sulfur contents and fractional abundances of reduced sulfur were adequate to allow similar formation of reduced sulfur-bound metals in all systems. The total solid-phase sulfur concentrations observed in the present work span the range reported in prior studies of freshwater subsurface aquatic systems (Casagrande et al., 1977; Altschuler et al., 1983; Brown, 1985; Wieder et al., 1985; Spratt and Morgan, 1990; Dail and Fitzgerald, 1999; Rozan et al., 2002; Prietzel et al., 2009; Mehlhorn et al., 2018), indicating that sulfur-bound trace metals have broad occurrences as key species in such systems regardless of the soil or sediment sulfur content.

4.2.2. Clay Minerals

Substantial prior work has demonstrated that nickel and zinc enter into clay mineral and layered double hydroxide structures in contaminated soils (Manceau et al., 2004; Voegelin et al., 2005; McNear et al., 2007; Jacquat et al., 2009; Voegelin et al., 2011), and this has also been observed for regions hosting Ni-rich ultramafic rocks (Dublet et al., 2012; Noël et al., 2015; Noël et al., 2017; Siebecker et al., 2017; Siebecker et al., 2018). However, the role of clay mineral structures in hosting trace metals in anoxic freshwater aquatic systems containing trace metals at low, background concentrations has not been previously demonstrated. The neoformation of such solids may depend on saturation state or dissolved metal concentrations (Manceau et al., 1999; Schlegel et al., 2001) and may be inhibited by organic matter (Nachtegaal and Sparks, 2003). This study demonstrates that the low trace metal contents of wetland soils and stream sediments still enable the incorporation of both nickel and zinc in clay structures, with this being the dominant nickel species in all systems. In addition, the occurrence of nickel and zinc in clay structures is independent of sulfur content and speciation, suggesting that they may be inherited from the weathering process and are resistant to disruption in the presence of sulfide.

4.3 Consistent Trace Metal Speciation in Wetland Soils and Stream Sediments

The study sites are distributed over a ~1000 km transect and represent different aquatic system types in geologically-distinct regions, with the marsh wetlands occurring in glacial sediments, the stream sediments draining carbonate and shale lithologies, and the riparian wetlands underlain by clastic coastal plain sediments. The riparian wetland soils are also heavily weathered compared to the other two sites, lacking smectite clay minerals at both study areas with no detectable feldspar at location Riparian 1, yielding more acidic and cation-poor local waters (Table

S1). Despite these substantial differences, the three sites investigated have overall similar trace metal speciation, with variations between the sampling locations at each site often larger than among the different field areas. These observations suggest that a small set of components consistently dominates trace metal speciation in uncontaminated freshwater subsurface aquatic systems: sulfide and adsorbed forms predominate in diverse systems for copper, with nickel and zinc also occurring in clay mineral structures. Further, similar distributions of trace metal species occur at multiple, unrelated and spatially separate field sites, which may indicate that these specific phase associations are a common feature of freshwater aquatic systems.

Limited prior studies of uncontaminated, anoxic soils and sediments generally support our hypothesis that trace metal speciation has consistent controls across many freshwater aquatic systems. A study of an anoxic soil and a peat lens formed at a natural CO_2 seep found copper bound primarily to reduced sulfur with a lesser component complexed to organic matter (Mehlhorn et al., 2018). As organic-complexed copper is classified into the adsorbed pool in the grouping scheme used in the present study, these results are consistent with our observations. Metallic copper was not observed by XANES in either our work or this prior study, suggesting it may be a substantial species only in contaminated flooded soils, where it has been frequently observed (Weber et al., 2009a; Fulda et al., 2013a; Hofacker et al., 2013b). Nickel forms sulfide and clay-associated species in anoxic coastal sediments (Noël et al., 2015; Noël et al., 2017; Merrot et al., 2019), which were also found in the present study. The greater importance of the sulfide species in these prior studies results from substantial pyrite formation caused by the reduction of the ample sulfate in seawater. These coastal systems are thus not directly comparable to freshwater aquatic systems, which typically have lower sulfate inputs (Wieder and Lang, 1988; Castro et al., 2002; Vile et al., 2003; Knorr and Blodau, 2009). However, locations within terrestrial-aquatic interfaces

where sulfur-rich groundwater mixes with fresh surface waters represent potential hot spots of reactivity which may require additional study. Further, these prior studies investigated systems with naturally elevated nickel concentrations (up to 0.5 wt.%) associated with an ultramafic laterite, potentially leading to distinct speciation. Despite these differences, the nickel sulfide pool was ubiquitous in the aquatic systems investigated here. This is likely supported by high rates of sulfate reduction in freshwater aquatic systems (Segarra et al., 2015) despite the lower total sulfate levels observed in the absence of seawater inputs. We are unaware of studies of zinc speciation in anoxic sites that are uncontaminated or lack geogenic zinc accumulations.

This study also highlights that the observations of trace metal behavior in contaminated systems often are not predictive of the behavior of these elements when they occur at natural, background levels. As noted above, metallic copper was not observed at any site in this study despite frequently being reported for contaminated soils (Weber et al., 2009a; Weber et al., 2009b; Fulda et al., 2013a; Hofacker et al., 2015). Similarly, our studies find that zinc sulfide is limited in occurrence, with zinc more commonly binding to reduced organic sulfur species. The greater abundance of zinc sulfide in contaminated settings (Bostick et al., 2001; Webb and Gaillard, 2015) may thus be more prevalent in systems receiving substantial zinc inputs.

Finally, this study suggests that greater insight into the speciation of trace metals occurring at geological background levels may be gained using modern analytical tools. The data obtained in this study for trace metals occurring at or below geological background levels was enabled by recent developments in detectors and enhancements in beam flux at synchrotron lightsources. This demonstrates that spectroscopic investigation of trace metal in other uncontaminated terrestrial aquatic systems is viable, allowing further evaluation of whether the consistent speciation observed in the present work is a general geochemical phenomenon.

5. CONCLUSIONS

Trace metals in marsh wetland soils, riparian wetland soils, and stream bed sediments at three field sites display a series of similar features. Relative solid-phase concentrations of trace metals followed the trend Zn > Cu ≈ Ni > Co, but their absolute abundance showed no predictive correlations with major element contents. Nickel, copper, and zinc all partially occurred as sulfur-bound species, yet the fractional abundance of these phases were insensitive to the bulk sulfur content, which varied by two orders of magnitude. Freshwater subsurface aquatic systems appear to contain adequate sulfur to stabilize sulfide minerals and metals complexed to reduced organic sulfur species despite their generally low total sulfur contents. Zinc and nickel also widely occurred in clay mineral structures, and all trace metals also occurred complexed to mineral surfaces and organic matter.

The lack of a relationship between sulfur-bound metal contents and total sulfur concentration may reflect the stability of other metal species or heterogeneous microenvironments in wetlands and stream beds. While reaction with iron might limit the availability of reduce sulfur to bind trace metals, it is difficult to envision how this would consistently generate similar fractions of metal-sulfur species across an array of soils and sediments. More broadly, similar species of each trace metal occurred in the soils and sediments at all field sites, often in similar proportions. The consistent trace metal speciation among distant and unrelated sites suggests that a small number of species may dominate freshwater wetland soils and stream sediments. Future investigation of the temporal dynamics of trace metal species in such settings may provide additional insight into the processes that yield consistent trace metal speciation across diverse freshwater aquatic systems.

Acknowledgements

This project was supported by U.S. Department of Energy, Office of Science, Office of Biological and Environmental Research, Subsurface Biogeochemical Research program through award no. DE-SC0019422 to Washington University and contract number DE-AC02-06CH11357 to Argonne National Laboratory for the Argonne Wetland Hydrobiogeochemistry Science Focus Area. Argonne National Laboratory is a U.S. Department of Energy laboratory managed by UChicago Argonne, LLC. This work was also supported by the Critical Interfaces Science Focus Area at Oak Ridge National Laboratory. Oak Ridge National Laboratory is managed by UT-Battelle, LLC, for the U.S. Department of Energy under contract DE-AC05-00OR22725. Work was conducted at the Savannah River National Laboratory under the U.S. Department of Energy Contract DE-AC09-96SR18500. N.S. was also supported by the McDonnell International Scholars Academy at Washington University. Portions of this research utilized the Stanford Synchrotron Radiation Lightsource (SSRL), SLAC National Accelerator Laboratory, which is supported by the U.S. Department of Energy (DOE), Office of Science, Office of Basic Energy Sciences under Contract No. DE-AC02-76SF00515, and the Advanced Photon Source, a U.S. DOE Office of Science User Facility, operated for the DOE Office of Science by Argonne National Laboratory under Contract No. DE-AC02-06CH11357. Ryan Davis is thanked for his assistance with beamline operations at SSRL. Preparation of select standards was performed by Ryan D. Nickerson, Kaushik Mitra, and Walter Schenkeveld. Associate Editor Owen Duckworth and four anonymous reviewers are thanked for detailed comments that improved this manuscript.

Appendix A. Supplementary Material

The Supplementary Materials include information on the synthesis and sources of standards for XANES and EXAFS analyses, a summary of surface water compositions and extractable nutrients,

886 a map of the field sites, plots of the standards used for XANES and EXAFS analyses, tabulations
887 of the chemical analyses and spectroscopic fitting results, and evidence for a zinc oxide
888 contaminant source.
889
890 **Research Data**
891 Research Data associated with this article can be accessed at https://doi.org/10.15485/1773008.
892

REFERENCES

Almkvist G., Boye K. and Persson I. (2010) K-edge XANES analysis of sulfur compounds: An investigation of the relative intensities using internal calibration. *J. Synchrotron Radiat.* **17**, 683–688.

Altschuler Z. S., Schnepfe M. M., Silber C. C. and Simon F. O. (1983) Sulfur diagenesis in everglades peat and origin of pyrite in coal. *Science* **221**, 221–227.

Arora B., Spycher N. F., Steefel C. I., Molins S., Bill M., Conrad M. E., Dong W., Faybishenko B., Tokunaga T. K., Wan J., Williams K. H. and Yabusaki S. B. (2016) Influence of hydrological, biogeochemical and temperature transients on subsurface carbon fluxes in a flood plain environment. *Biogeochemistry* **127**, 367–396.

Basiliko N. and Yavitt J. B. (2001) Influence of Ni, Co, Fe, and Na additions on methane production in *Sphagnum*-dominated Northern American peatlands. *Biogeochemistry* **52**, 133–153.

Bethke C. M. (2007) *Geochemical and biogeochemical reaction modeling*, 2nd Ed. Cambridge University Press, Cambridge.

Bostick B. C., Hansel C. M., La Force M. J. and Fendorf S. (2001) Seasonal fluctuations in zinc speciation within a contaminated wetland. *Environ. Sci. Technol.* **35**, 3823–3829.

Bouwman A. F., Beusen A. H. W., Griffioen J., Van Groenigen J. W., Hefting M. M., Oenema O., Van Puijenbroek P. J. T. M., Seitzinger S., Slomp C. P. and Stehfest E. (2013) Global trends and uncertainties in terrestrial denitrification and N_2O emissions. *Philos. Trans. R. Soc. B Biol. Sci.* **368**.

Bowden W. B. (1987) The biogeochemistry of nitrogen in freshwater wetlands. *Biogeochemistry* **4**, 313–348.

Brooks S. C. and Southworth G. R. (2011) History of mercury use and environmental contamination at the Oak Ridge Y-12 Plant. *Environ. Pollut.* **159**, 219–228.

Brown K. A. (1985) Sulphur distribution and metabolism in waterlogged peat. *Soil Biol. Biochem.* **17**, 39–45.

Brown K., Tegoni M., Prudêncio M., Pereira A. S., Besson S., Moura J. J., Moura I. and Cambillau C. (2000) A novel type of catalytic copper cluster in nitrous oxide reductase. *Nat. Struct. Biol.* **7**, 191–195.

Caritat P. de, Reimann C., Smith D. B. and Wang X. (2018) Chemical elements in the environment: Multi-element geochemical datasets from continental- to national-scale surveys on four continents. *Appl. Geochemistry* **89**, 150–159.

Casagrande D. J., Siefert K., Berschinski C. and Sutton N. (1977) Sulfur in peat-forming systems of the Okefenokee Swamp and Florida Everglades: origins of sulfur in coal. *Geochim. Cosmochim. Acta* **41**, 161–167.

Castro H., Reddy K. R. and Ogram A. (2002) Composition and function of sulfate-reducing prokaryotes in eutrophic and pristine areas of the Florida Everglades. *Appl. Environ. Microbiol.* **68**, 6129–6137.

Cervi E. C., Clark S., Boye K. E., Gustafsson J. P., Baken S. and Burton G. A. (2021) Copper transformation, speciation, and detoxification in anoxic and suboxic freshwater sediments. *Chemosphere* **282**, 131063.

Dähn R., Scheidegger A. M., Manceau A., Schlegel M. L., Baeyens B., Bradbury M. H. and Morales M. (2002) Neoformation of Ni phyllosilicate upon Ni uptake on montmorillonite: A kinetics study by powder and polarized extended X-ray absorption fine structure spectroscopy. *Geochim. Cosmochim. Acta* **66**, 2335–2347.

939 Dail D. B. and Fitzgerald J. W. (1999) S Cycling in soil and stream sediment: Influence of
940 season and in situ concentrations of carbon, nitrogen and sulfur. *Soil Biol. Biochem.* **31**,
941 1395–1404.
942 Danczak R. E., Sawyer A. H., Williams K. H., Stegen J. C., Hobson C. and Wilkins M. J. (2016)
943 Seasonal hyporheic dynamics control coupled microbiology and geochemistry in Colorado
944 River sediments. *J. Geophys. Res. Biogeosciences* **121**, 2976–2987.
945 Delaney J. and Lundeen S. (1990) The LLNL thermodynamical database. Lawrence Livermore
946 National Laboratory Report UCRL-21658, 150 pp.
947 Donovan P. M., Blum J. D., Demers J. D., Gu B., Brooks S. C. and Peryam J. (2014)
948 Identification of multiple mercury sources to stream sediments near Oak Ridge, TN, USA.
949 *Environ. Sci. Technol.* **48**, 3666–3674.
950 Dublet G., Juillot F., Morin G., Fritsch E., Fandeur D., Ona-Nguema G. and Brown G. E., Jr.
951 (2012) Ni speciation in a New Caledonian lateritic regolith: A quantitative X-ray absorption
952 spectroscopy investigation. *Geochim. Cosmochim. Acta* **95**, 119–133.
953 Ekstrom E. B. and Morel F. M. M. (2008) Cobalt limitation of growth and mercury methylation
954 in sulfate-reducing bacteria. *Environ. Sci. Technol.* **42**, 93–99.
955 Van Der Ent A., Mak R., De Jonge M. D. and Harris H. H. (2018) Simultaneous
956 hyperaccumulation of nickel and cobalt in the tree *Glochidion* cf. *sericeum*
957 (Phyllanthaceae): Elemental distribution and chemical speciation. *Sci. Rep.* **8**, 9683.
958 Ermler U., Grabarse W., Shima S., Goubeaud M. and Thauer R. K. (1997) Crystal structure of
959 methyl-coenzyme M reductase: The key enzyme of biological methane formation. *Science*
960 **278**, 1457–1462.
961 Falkowski P. G., Barber R. T. and Smetacek V. (1998) Biogeochemical controls and feedbacks
962 on ocean primary production. *Science* **281**, 200–206.
963 Flynn T. M., Koval J. C., Greenwald S. M., Owens S. M., Kemner K. M. and Antonopoulos D.
964 A. (2017) Parallelized, aerobic, single carbon-source enrichments from different natural
965 environments contain divergent microbial communities. *Front. Microbiol.* **8**, 2321.
966 Flynn T. M., O'Loughlin E. J., Mishra B., DiChristina T. J. and Kemner K. M. (2014) Sulfur-
967 mediated electron shuttling during bacterial iron reduction. *Science* **344**, 1039–1042.
968 Ford R. G. and Sparks D. L. (2000) The nature of Zn precipitates formed in the presence of
969 pyrophyllite. *Environ. Sci. Technol.* **34**, 2479–2483.
970 Fulda B., Voegelin A., Ehlert K. and Kretzschmar R. (2013a) Redox transformation, solid phase
971 speciation and solution dynamics of copper during soil reduction and reoxidation as affected
972 by sulfate availability. *Geochim. Cosmochim. Acta* **123**, 385–402.
973 Fulda B., Voegelin A., Maurer F., Christl I. and Kretzschmar R. (2013b) Copper redox
974 transformation and complexation by reduced and oxidized soil humic acid. 1. X-ray
975 absorption spectroscopy study. *Environ. Sci. Technol.* **47**, 10903–10911.
976 Gärtner P., Ecker A., Fischer R., Linder D., Fuchs G. and Thauer R. K. (1993) Purification and
977 properties of N^5-methyltetrahydromethanopterin: coenzyme M methyltransferase from
978 *Methanobacterium thermoautotrophicum*. *Eur. J. Biochem.* **213**, 537–545.
979 George G. N., Gnida M., Bazylinski D. A., Prince R. C. and Pickering I. J. (2008) X-ray
980 absorption spectroscopy as a probe of microbial sulfur biochemistry: The nature of bacterial
981 sulfur globules revisited. *J. Bacteriol.* **190**, 6376–6383.
982 Glass J. B. and Orphan V. J. (2012) Trace metal requirements for microbial enzymes involved in
983 the production and consumption of methane and nitrous oxide. *Front. Microbiol.* **3**, 1–20.
984 Glatzel S., Forbrich I., Krüger C., Lemke S. and Gerold G. (2008) Small scale controls of

greenhouse gas release under elevated N deposition rates in a restoring peat bog in NW Germany. *Biogeosciences* **5**, 925–935.
Glodowska M., Stopelli E., Schneider M., Rathi B., Straub D., Lightfoot A., Kipfer R., Berg M., Jetten M. and Kleindienst S. (2020) Arsenic mobilization by anaerobic iron-dependent methane oxidation. *Commun. Earth Environ.* **1**, 1–7.
Granger J. and Ward B. B. (2003) Accumulation of nitrogen oxides in copper-limited cultures of denitrifying bacteria. *Limnol. Oceanogr.* **48**, 313–318.
Graulis S., Chateigner D., Downs R. T., Yokochi A. F. T., Quirós M., Lutterotti L., Manakova E., Butkus J., Moeck P. and Le Bail A. (2009) Crystallography Open Database - An open-access collection of crystal structures. *J. Appl. Crystallogr.* **42**, 726–729.
Groffman P. M., Gold A. J. and Jacinthe P. A. (1998) Nitrous oxide production in riparian zones and groundwater. *Nutr. Cycl. Agroecosystems* **52**, 179–186.
Hansel C. M., Lentini C. J., Tang Y., Johnston D. T., Wankel S. D. and Jardine P. M. (2015) Dominance of sulfur-fueled iron oxide reduction in low-sulfate freshwater sediments. *ISME J.* **9**, 2400–2412.
Harmsen J. (2007) Measuring bioavailability: From a scientific approach to standard methods. *J. Environ. Qual.* **36**, 1420–1428.
Hassan N. M., Rasmussen P. E., Dabek-Zlotorzynska E., Celo V. and Chen H. (2007) Analysis of environmental samples using microwave-assisted acid digestion and inductively coupled plasma mass spectrometry: Maximizing total element recoveries. *Water. Air. Soil Pollut.* **178**, 323–334.
Hlaváčová E., Rulík M. and Čáp L. (2005) Anaerobic microbial metabolism in hyporheic sediment of a gravel bar in a small lowland stream. *River Res. Appl.* **21**, 1003–1011.
Hofacker A. F., Behrens S., Voegelin A., Kaegi R., Lösekann-Behrens T., Kappler A. and Kretzschmar R. (2015) *Clostridium* species as metallic copper-forming bacteria in soil under reducing conditions. *Geomicrobiol. J.* **32**, 130–139.
Hofacker A. F., Voegelin A., Kaegi R. and Kretzschmar R. (2013a) Mercury mobilization in a flooded soil by incorporation into metallic copper and metal sulfide nanoparticles. *Environ. Sci. Technol.* **47**, 7739–7746.
Hofacker A. F., Voegelin A., Kaegi R., Weber F. A. and Kretzschmar R. (2013b) Temperature-dependent formation of metallic copper and metal sulfide nanoparticles during flooding of a contaminated soil. *Geochim. Cosmochim. Acta* **103**, 316–332.
Huerta-Diaz M. A., Tessier A. and Carignan R. (1998) Geochemistry of trace metals associated with reduced sulfur in freshwater sediments. *Appl. Geochemistry* **13**, 213–233.
Jacquat O., Voegelin A. and Kretzschmar R. (2009) Soil properties controlling Zn speciation and fractionation in contaminated soils. *Geochim. Cosmochim. Acta* **73**, 5256–5272.
Jacquot J. E., Horak R. E. A., Amin S. A., Devol A. H., Ingalls A. E., Armbrust E. V., Stahl D. A. and Moffett J. W. (2014) Assessment of the potential for copper limitation of ammonia oxidation by Archaea in a dynamic estuary. *Mar. Chem.* **162**, 37–49.
Janot N., Lezama Pacheco J. S., Pham D. Q., O'Brien T. M., Hausladen D., Noël V., Lallier F., Maher K., Fendorf S., Williams K. H., Long P. E. and Bargar J. R. (2016) Physico-chemical heterogeneity of organic-rich sediments in the Rifle Aquifer, CO: Impact on uranium biogeochemistry. *Environ. Sci. Technol.* **50**, 46–53.
Kaplan D. I., Smith R., Parker C. J., Baker M., Cabrera T., Ferguson B. O., Kemner K. M., Laird M., Logan C., Lott J., Manglass L., Martinez N. E., Montgomery D., Seaman J. C., Shapiro M. and Powell B. A. (2020) Uranium attenuated by a wetland 50 years after release into a

stream. *ACS Earth Sp. Chem.* **4**, 1360–1366.
Kelly S. D., Hesterberg D. and Ravel B. (2008) Analysis of soils and minerals using X-ray absorption spectroscopy. In *Methods of Soil Analysis Part 5 - Mineralogical Methods* (eds. A.L. Ulery and L.R. Drees). Soil Science Society of America, Madison. pp. 387–463.
Kirschke S., Bousquet P., Ciais P., Saunois M., Canadell J. G., Dlugokencky E. J., Bergamaschi P., Bergmann D., Blake D. R., Bruhwiler L., Cameron-Smith P., Castaldi S., Chevallier F., Feng L., Fraser A., Heimann M., Hodson E. L., Houweling S., Josse B., Fraser P. J., Krummel P. B., Lamarque J. F., Langenfelds R. L., Le Quéré C., Naik V., O'doherty S., Palmer P. I., Pison I., Plummer D., Poulter B., Prinn R. G., Rigby M., Ringeval B., Santini M., Schmidt M., Shindell D. T., Simpson I. J., Spahni R., Steele L. P., Strode S. A., Sudo K., Szopa S., Van Der Werf G. R., Voulgarakis A., Van Weele M., Weiss R. F., Williams J. E. and Zeng G. (2013) Three decades of global methane sources and sinks. *Nat. Geosci.* **6**, 813–823.
Knorr K. H. and Blodau C. (2009) Impact of experimental drought and rewetting on redox transformations and methanogenesis in mesocosms of a northern fen soil. *Soil Biol. Biochem.* **41**, 1187–1198.
Kocar B. D. and Fendorf S. (2009) Thermodynamic constraints on reductive reactions influencing the biogeochemistry of arsenic in soils and sediments. *Environ. Sci. Technol.* **43**, 4871–4877.
Kopittke P. M., Menzies N. W., de Jonge M. D., Mckenna B. A., Donner E., Webb R. I., Paterson D. J., Howard D. L., Ryan C. G., Glover C. J., Scheckel K. G. and Lombi E. (2011) In situ distribution and speciation of toxic copper, nickel, and zinc in hydrated roots of cowpea. *Plant Physiol.* **156**, 663–673.
Koretsky C. M., Haveman M., Beuving L., Cuellar A., Shattuck T. and Wagner M. (2007) Spatial variation of redox and trace metal geochemistry in a minerotrophic fen. *Biogeochemistry* **86**, 33–62.
Koretsky C. M., Moore C. M., Lowe K. L., Meile C., Dichristina T. J. and Van Cappellen P. (2003) Seasonal oscillation of microbial iron and sulfate reduction in saltmarsh sediments (Sapelo Island, GA, USA). *Biogeochemistry* **64**, 179–203.
LaRowe D. E. and Van Cappellen P. (2011) Degradation of natural organic matter: A thermodynamic analysis. *Geochim. Cosmochim. Acta* **75**, 2030–2042.
Lau G. E., Cosmidis J., Grasby S. E., Trivedi C. B., Spear J. R. and Templeton A. S. (2017) Low-temperature formation and stabilization of rare allotropes of cyclooctasulfur (β-S_8 and γ-S_8) in the presence of organic carbon at a sulfur-rich glacial site in the Canadian High Arctic. *Geochim. Cosmochim. Acta* **200**, 218–231.
Lett R. E. W. and Fletcher W. K. (1980) Syngenetic sulphide minerals in a copper-rich bog. *Miner. Depos.* **15**, 61–67.
Van Lonkhuyzen R. A. and LaGory K. E. (1994) *Wetlands of Argonne National Laboratory-East DuPage County, Illinois*. Argonne National Laboratory Report ANL/EAD/TM-12, 46 pp.
Van Lonkhuyzen R. A., Lagory K. E. and Kuiper J. A. (2004) Modeling the suitability of potential wetland mitigation sites with a geographic information system. *Environ. Manage.* **33**, 368–375.
Lu X., Johs A., Zhao L., Wang L., Pierce E. M. and Gu B. (2018) Nanomolar copper enhances mercury methylation by *Desulfovibrio desulfuricans* ND132. *Environ. Sci. Technol. Lett.* **5**, 372–376.
Manceau A., Marcus M. A. and Tamura N. (2002) Quantitative speciation of heavy metals in

soils and sediments by synchrotron X-ray techniques. *Rev. Mineral. Geochem.* **49**, 341–428.
Manceau A., Marcus M. A., Tamura N., Proux O., Geoffroy N. and Lanson B. (2004) Natural speciation of Zn at the micrometer scale in a clayey soil using X-ray fluorescence, absorption, and diffraction. *Geochim. Cosmochim. Acta* **68**, 2467–2483.
Manceau A. and Nagy K. L. (2012) Quantitative analysis of sulfur functional groups in natural organic matter by XANES spectroscopy. *Geochim. Cosmochim. Acta* **99**, 206–223.
Manceau A., Schlegel M., Nagy K. L. and Charlet L. (1999) Evidence for the formation of trioctahedral clay upon sorption of Co^{2+} on quartz. *J. Colloid Interface Sci.* **220**, 181–197.
Manceau A., Tommaseo C., Rihs S., Geoffroy N., Chateigner D., Schlegel M., Tisserand D., Marcus M. A., Tamura N. and Chen Z. S. (2005) Natural speciation of Mn, Ni, and Zn at the micrometer scale in a clayey paddy soil using X-ray fluorescence, absorption, and diffraction. *Geochim. Cosmochim. Acta* **69**, 4007–4034.
Mantha H., Schindler M. and Hochella M. F. (2019) Occurrence and formation of incidental metallic Cu and CuS nanoparticles in organic-rich contaminated surface soils in Timmins, Ontario. *Environ. Sci. Nano* **6**, 163–179.
McClain M. E., Boyer E. W., Dent C. L., Gergel S. E., Grimm N. B., Groffman P. M., Hart S. C., Harvey J. W., Johnston C. A., Mayorga E., McDowell W. H. and Pinay G. (2003) Biogeochemical hot spots and hot moments at the interface of terrestrial and aquatic ecosystems. *Ecosystems* **6**, 301–312.
McNear D. H., Chaney R. L. and Sparks D. L. (2007) The effects of soil type and chemical treatment on nickel speciation in refinery enriched soils: A multi-technique investigation. *Geochim. Cosmochim. Acta* **71**, 2190–2208.
Mehlhorn J., Besold J., Lezama Pacheco J. S., Gustafsson J. P., Kretzschmar R. and Planer-Friedrich B. (2018) Copper mobilization and immobilization along an organic matter and redox gradient - Insights from a Mofette Site. *Environ. Sci. Technol.* **52**, 13698–13707.
Merrot P., Juillot F., Noël V., Lefebvre P., Brest J., Menguy N., Guigner J. M., Blondeau M., Viollier E., Fernandez J. M., Moreton B., Bargar J. R. and Morin G. (2019) Nickel and iron partitioning between clay minerals, Fe-oxides and Fe-sulfides in lagoon sediments from New Caledonia. *Sci. Total Environ.* **689**, 1212–1227.
Nachtegaal M., Scheidegger A. M., Dähn R., Chateigner D. and Furrer G. (2005) Immobilization of Ni by Al-modified montmorillonite: A novel uptake mechanism. *Geochim. Cosmochim. Acta* **69**, 4211–4225.
Nachtegaal M. and Sparks D. L. (2003) Nickel sequestration in a kaolinite-humic acid complex. *Environ. Sci. Technol.* **37**, 529–534.
Neumann R. B., Blazewicz S. J., Conaway C. H., Turetsky M. R. and Waldrop M. P. (2016) Modeling CH_4 and CO_2 cycling using porewater stable isotopes in a thermokarst bog in Interior Alaska: results from three conceptual reaction networks. *Biogeochemistry* **127**, 57–87.
Newville M. (2001) IFEFFIT: Interactive XAFS analysis and FEFF fitting. *J. Synchrotron Radiat.* **8**, 322–324.
Noël V., Juillot F., Morin G., Marchand C., Ona-Nguema G., Viollier E., Prévot F., Dublet G., Maillot F., Delbes L., Marakovic G., Bargar J. R. and Brown G. E. (2017) Oxidation of Ni-rich mangrove sediments after isolation from the sea (Dumbea Bay, New Caledonia): Fe and Ni behavior and environmental implications. *ACS Earth Sp. Chem.* **1**, 455–464.
Noël V., Morin G., Juillot F., Marchand C., Brest J., Bargar J. R., Muñoz M., Marakovic G., Ardo S. and Brown G. E. (2015) Ni cycling in mangrove sediments from New Caledonia.

Geochim. Cosmochim. Acta **169**, 82–98.
Pansu M. and Gautheyrou J. (2006) *Handbook of soil analysis: Mineralogical, organic and inorganic methods*. Springer-Verlag, Berlin Heidelberg.
Parks J. M., Johs A., Podar M., Bridou R., Hurt R. A., Smith S. D., Tomanicek S. J., Qian Y., Brown S. D., Brandt C. C., Palumbo A. V., Smith J. C., Wall J. D., Elias D. A. and Liang L. (2013) The genetic basis for bacterial mercury methylation. *Science* **339**, 1332–1335.
Prietzel J., Thieme J., Tyufekchieva N., Paterson D., McNulty I. and Kögel-Knabner I. (2009) Sulfur speciation in well-aerated and wetland soils in a forested catchment assessed by sulfur K-edge X-ray absorption near-edge spectroscopy (XANES). *J. Plant Nutr. Soil Sci.* **172**, 393–403.
Ratié G., Garnier J., Calmels D., Vantelon D., Guimarães E., Monvoisin G., Nouet J., Ponzevera E. and Quantin C. (2018) Nickel distribution and isotopic fractionation in a Brazilian lateritic regolith: Coupling Ni isotopes and Ni K-edge XANES. *Geochim. Cosmochim. Acta* **230**, 137–154.
Ravel B. and Newville M. (2005) ATHENA, ARTEMIS, HEPHAESTUS: Data analysis for X-ray absorption spectroscopy using IFEFFIT. *J. Synchrotron Radiat.* **12**, 537–541.
Riscassi A., Miller C. and Brooks S. (2016) Seasonal and flow-driven dynamics of particulate and dissolved mercury and methylmercury in a stream impacted by an industrial mercury source. *Environ. Toxicol. Chem.* **35**, 1386–1400.
Rozan T. F., Taillefert M., Trouwborst R. E., Glazer B. T., Ma S., Herszage J., Valdes L. M., Price K. S. and Luther G. W. (2002) Iron-sulfur-phosphorus cycling in the sediments of a shallow coastal bay: Implications for sediment nutrient release and benthic macroalgal blooms. *Limnol. Oceanogr.* **47**, 1346–1354.
Rudnick R. L. and Gao S. (2003) Composition of the continental crust In *Treatise on Geochemistry* (eds. K.K. Turekian and H.D. Holland). In *Treatise on Geochemistry. Pergamon, Oxford* Elsevier. pp. 1–64.
Schaefer J. K., Kronberg R. M., Morel F. M. M. and Skyllberg U. (2014) Detection of a key Hg methylation gene, *hgcA*, in wetland soils. *Environ. Microbiol. Rep.* **6**, 441–447.
Schlegel M. L., Manceau A., Charlet L., Chateigner D. and Hazemann J. L. (2001) Sorption of metal ions on clay minerals. III. Nucleation and epitaxial growth of Zn phyllosilicate on the edges of hectorite. *Geochim. Cosmochim. Acta* **65**, 4155–4170.
Schönheit P., Moll J. and Thauer R. K. (1979) Nickel, cobalt, and molybdenum requirement for growth of *Methanobacterium thermoautotrophicum*. *Arch. Microbiol.* **123**, 105–107.
Schwartz G. E., Olsen T. A., Muller K. A. and Brooks S. C. (2019) Ecosystem controls on methylmercury production by periphyton biofilms in a contaminated stream: Implications for predictive modeling. *Environ. Toxicol. Chem.* **38**, 2426–2435.
Segarra K. E. A., Schubotz F., Samarkin V., Yoshinaga M. Y., Hinrichs K. U. and Joye S. B. (2015) High rates of anaerobic methane oxidation in freshwater wetlands reduce potential atmospheric methane emissions. *Nat. Commun.* **6**, 7477.
Siebecker M. G., Chaney R. L. and Sparks D. L. (2018) Natural speciation of nickel at the micrometer scale in serpentine (ultramafic) topsoils using microfocused X-ray fluorescence, diffraction, and absorption. *Geochem. Trans.* **19**, 14.
Siebecker M. G., Chaney R. L. and Sparks D. L. (2017) Nickel speciation in several serpentine (ultramafic) topsoils via bulk synchrotron-based techniques. *Geoderma* **298**, 35–45.
Singer M. B., Harrison L. R., Donovan P. M., Blum J. D. and Marvin-DiPasquale M. (2016) Hydrologic indicators of hot spots and hot moments of mercury methylation potential along

river corridors. *Sci. Total Environ.* **568**, 697–711.
Skyllberg U. (2008) Competition among thiols and inorganic sulfides and polysulfides for Hg and MeHg in wetland soils and sediments under suboxic conditions: Illumination of controversies and implications for MeHg net production. *J. Geophys. Res. Biogeosciences* **113**, G00C03.
Southworth G., Mathews T., Greeley M., Peterson M., Brooks S. and Ketelle D. (2013) Sources of mercury in a contaminated stream-implications for the timescale of recovery. *Environ. Toxicol. Chem.* **32**, 764–772.
Sparks D. L., Page A. L., Helmke P. A., Loeppert R. H., N. S. P., Tabatabai M. A., T. J. C. and Sumner M. E. (1996) *Methods of soil analysis Part 3 - Chemical Methods*. Soil Science Society of America, Madison.
Spratt H. G. and Morgan M. D. (1990) Sulfur cycling in a cedar-dominated, freshwater wetland. *Limnol. Oceanogr.* **35**, 1586–1593.
St Louis V. L., Rudd J. W. M., Kelly C. A., Beaty K. G., Bloom N. S. and Flett R. J. (1994) Importance of wetlands as sources of methyl mercury to boreal forest ecosystems. *Can. J. Fish. Aquat. Sci.* **51**, 1065–1076.
Sun L., Zheng C., Yang J., Peng C., Xu C., Wang Y., Feng J. and Shi J. (2016) Impact of sulfur (S) fertilization in paddy soils on copper (Cu) accumulation in rice (*Oryza sativa* L.) plants under flooding conditions. *Biol. Fertil. Soils* **52**, 31–39.
Swanner E. D., Webb S. M. and Kappler A. (2019) Fate of cobalt and nickel in mackinawite during diagenetic pyrite formation. *Am. Mineral.* **104**, 917–928.
Thauer R. K. (1998) Biochemistry of methanogenesis: a tribute to Marjory Stephenson:1998 Marjory Stephenson Prize Lecture. *Microbiology* **144**, 2377–2406.
Thirumalai K., Singh A. and Ramesh R. (2011) A MATLAB^{TM} code to perform weighted linear regression with (correlated or uncorrelated) errors in bivariate data. *J. Geol. Soc. India* **77**, 377–380.
Tian H., Chen G., Lu C., Xu X., Ren W., Zhang B., Banger K., Tao B., Pan S., Liu M., Zhang C., Bruhwiler L. and Wofsy S. (2015) Global methane and nitrous oxide emissions from terrestrial ecosystems due to multiple environmental changes. *Ecosyst. Heal. Sustain.* **1**, 1–20.
Vile M. A., Bridgham S. D., Wieder R. K. and Novák M. (2003) Atmospheric sulfur deposition alters pathways of gaseous carbon production in peatlands. *Global Biogeochem. Cycles* **17**.
Voegelin A., Jacquat O., Pfister S., Barmettler K., Scheinost A. C. and Kretzschmar R. (2011) Time-dependent changes of zinc speciation in four soils contaminated with zincite or sphalerite. *Environ. Sci. Technol.* **45**, 255–261.
Voegelin A., Pfister S., Scheinost A. C., Marcus M. A. and Kretzschmar R. (2005) Changes in zinc speciation in field soil after contamination with zinc oxide. *Environ. Sci. Technol.* **39**, 6616–6623.
Webb S. M. (2005) SIXpack: A graphical user interface for XAS analysis using IFEFFIT. *Phys. Scr. T* **T115**, 1011–1014.
Webb S. M. and Gaillard J. F. (2015) Zinc speciation in contaminated sediments: quantitative determination of zinc coordination by X-ray absorption spectroscopy. *Aquat. Geochemistry* **21**, 295–312.
Weber F. A., Voegelin A., Kaegi R. and Kretzschmar R. (2009a) Contaminant mobilization by metallic copper and metal sulphide colloids in flooded soil. *Nat. Geosci.* **2**, 267–271.
Weber F. A., Voegelin A. and Kretzschmar R. (2009b) Multi-metal contaminant dynamics in

temporarily flooded soil under sulfate limitation. *Geochim. Cosmochim. Acta* **73**, 5513–5527.

Weber K. A., Urrutia M. M., Churchill P. F., Kukkadapu R. K. and Roden E. E. (2006) Anaerobic redox cycling of iron by freshwater sediment microorganisms. *Environ. Microbiol.* **8**, 100–113.

Wieder R. K. and Lang G. E. (1988) Cycling of inorganic and organic sulfur in peat from Big Run Bog, West Virginia. *Biogeochemistry* **5**, 221–242.

Wieder R. K., Lang G. E. and Granus V. A. (1985) An evaluation of wet chemical methods for quantifying sulfur fractions in freshwater wetland peat. *Limnol. Oceanogr.* **30**, 1109–1115.

Williams A. G. B., Scheckel K. G., McDermott G., Gratson D., Neptune D. and Ryan J. A. (2011) Speciation and bioavailability of zinc in amended sediments. *Chem. Speciat. Bioavailab.* **23**, 143–154.

Woodward G. L., Peacock C. L., Otero-Fariña A., Thompson O. R., Brown A. P. and Burke I. T. (2018) A universal uptake mechanism for cobalt(II) on soil constituents: Ferrihydrite, kaolinite, humic acid, and organo-mineral composites. *Geochim. Cosmochim. Acta* **238**, 270–291.

Worms I., Simon D. F., Hassler C. S. and Wilkinson K. J. (2006) Bioavailability of trace metals to aquatic microorganisms: importance of chemical, biological and physical processes on biouptake. *Biochimie* **88**, 1721–1731.

Xia B., Qiu H., Knorr K. H., Blodau C. and Qiu R. (2018) Occurrence and fate of colloids and colloid-associated metals in a mining-impacted agricultural soil upon prolonged flooding. *J. Hazard. Mater.* **348**, 56–66.

Yang J., Zhu S., Zheng C., Sun L., Liu J. and Shi J. (2015) Impact of S fertilizers on pore-water Cu dynamics and transformation in a contaminated paddy soil with various flooding periods. *J. Hazard. Mater.* **286**, 432–439.

Yang Z., Fang W., Lu X., Sheng G. P., Graham D. E., Liang L., Wullschleger S. D. and Gu B. (2016) Warming increases methylmercury production in an Arctic soil. *Environ. Pollut.* **214**, 504–509.

Yoon S.-J., Yáñez C., Bruns M. A., Martínez-Villegas N. and Martínez C. E. (2012) Natural zinc enrichment in peatlands: Biogeochemistry of ZnS formation. *Geochim. Cosmochim. Acta* **84**, 165–176.

Zarnetske J. P., Haggerty R., Wondzell S. M. and Baker M. A. (2011) Dynamics of nitrate production and removal as a function of residence time in the hyporheic zone. *J. Geophys. Res. Biogeosciences* **116**, G01025.

Zhang Z., Zimmermann N. E., Stenke A., Li X., Hodson E. L., Zhu G., Huang C. and Poulter B. (2017) Emerging role of wetland methane emissions in driving 21st century climate change. *Proc. Natl. Acad. Sci. U. S. A.* **114**, 9647–9652.

Zhao C. M., Campbell P. G. C. and Wilkinson K. J. (2016) When are metal complexes bioavailable? *Environ. Chem.* **13**, 425–433.

Zheng K., Ngo P. D., Owens V. L., Yang X. P. and Mansoorabadi S. O. (2016) The biosynthetic pathway of coenzyme F430 in methanogenic and methanotrophic archaea. *Science* **354**, 339–342.

TABLES

Table 1. Sample depth (cm) for soil and sediment core segments.

Sample Location	C1-1	C1-2	C2-1	C2-2
Marsh 1	0-7.5	7.5-15.3	0-9	9-18.4
Marsh 2	0-6.5	6.5-11	0-9	9-12
Riparian 1	0-4.5	4.5-9.5	0-4.5	4.5-10.5
Riparian 2	0-4.5	4.5-9.5	0-4	4-10
Stream 1	0-8	8-21.5	0-3	3-19.5
Stream 2*	0-8	8-12	0-8	8-18

*A third segment was obtained for C2 from this location over the depth range of 18 to 28.5 cm.

FIGURE CAPTIONS

Figure 1. Powder X-ray diffraction (XRD) patterns of the surface soil or sediment layer over the full range (top) or the low angle region more sensitive to clay minerals. Data for duplicate cores are shown for location Stream 1 because of their distinct mineralogy.

Figure 2. Total carbon, sulfur, iron, and manganese contents in the surface layer of the soils and sediments at the study sites. The error bars reflect the standard deviations of triplicate analyses of samples of individual cores added in quadrature to the standard deviation of the mean values for the two duplicate cores collected at each site (Data tabulated in Table S6).

Figure 3. Dissolved (top) and total solid phase (bottom) trace metal concentrations for the study sites. The error bars for the dissolved concentrations are the uncertainties of individual analyses obtained from linear regression of the calibration curves. Error bars from the solid phase concentration reflect the calibration-derived uncertainties for samples from individual cores added in quadrature to the standard deviation of the mean values for the two duplicate cores collected at each site (Data tabulated in Tables S3 and S4).

Figure 4. Sulfur K edge XANES spectra (solid) and fits (dashed) and the associated distribution of species for the surface layer soils and sediments at the study locations (Results tabulated in Table S12).

Figure 5. Iron K-edge XANES (top) and EXAFS (bottom) spectra (solid) and fits (dashed) and the associated distribution of species for the surface layer soils and sediments at the study locations. (Results tabulated in Tables S13 and S14)

Figure 6. Cu-K edge XANES spectra (solid) and fits (dashed) and the associated distribution of species for the surface layer soils and sediments at the study locations (Results tabulated in Table S15).

Figure 7. Ni-K edge XANES spectra (solid) and fits (dashed) and the associated distribution of species for the surface layer soils and sediments at the study locations (Results tabulated in Table S16).

Figure 8. Zn-K edge XANES spectra (solid) and fits (dashed) and the associated distribution of species for the surface layer soils and sediments at the study locations (Results tabulated in Table S17).

Figure 9. Correlation coefficients (R) and associated p-values derived from weighted linear regression of the solid-phase concentrations of each element pair. Data for the stream bed site excluded the single sample containing pyrite.

Figure 10. (A) Average and standard deviation of the fraction of trace metals bound to reduced sulfur as determined by XANES spectroscopy. (B) Variation in the fraction of each trace metal bound to reduced sulfur compared to the total sulfur content of the samples compared to trend lines for each metal (Cu: $R = -0.06$, $p = 0.03$; Ni: $R = 0.37$, $p = 0.001$; Zn: $R = 0.18$, $p = 0.1$) determined through linear regression weighted by the bivariate uncertainties.

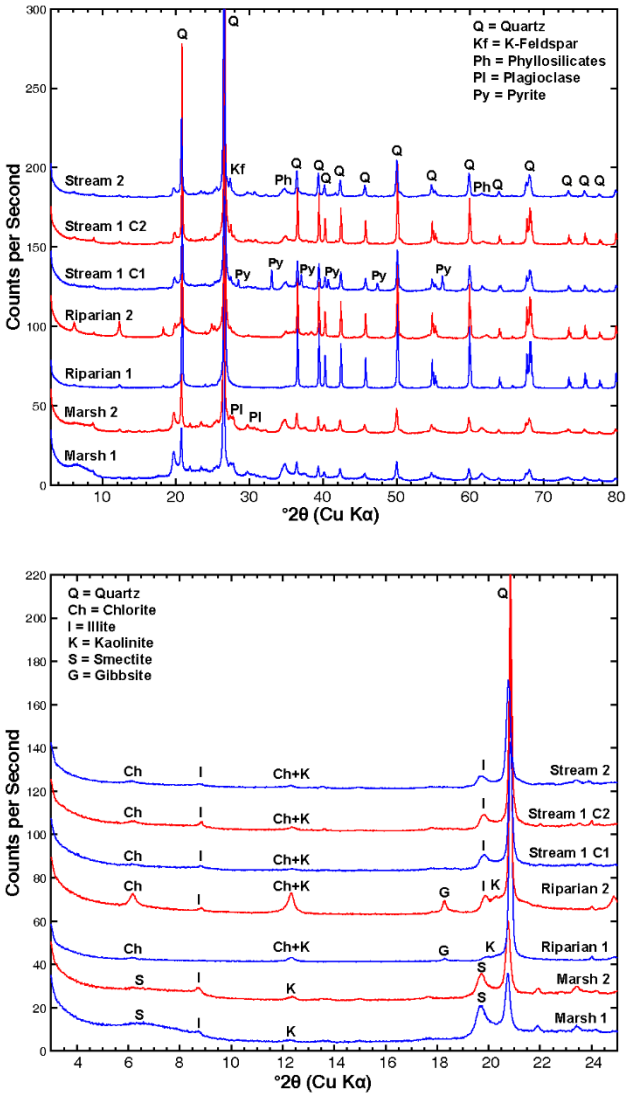

Figure 1. Powder X-ray diffraction (XRD) patterns of the surface soil or sediment layer over the full range (top) or the low angle region more sensitive to clay minerals. Data for duplicate cores are shown for location Stream 1 because of their distinct mineralogy.

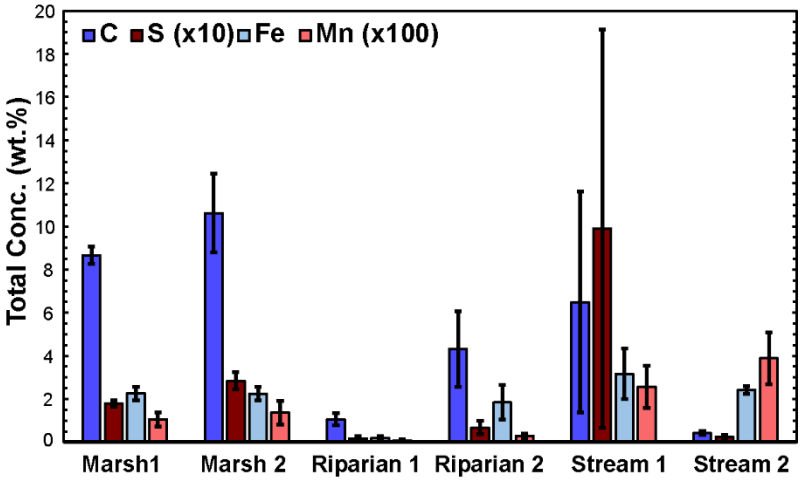

1317

1318 **Figure 2.** Total carbon, sulfur, iron, and manganese contents in the surface layer of the soils and

1319 sediments at the study sites. The error bars reflect the standard deviations of triplicate analyses of

1320 samples of individual cores added in quadrature to the standard deviation of the mean values for

1321 the two duplicate cores collected at each site (Data tabulated in Table S6).

1322

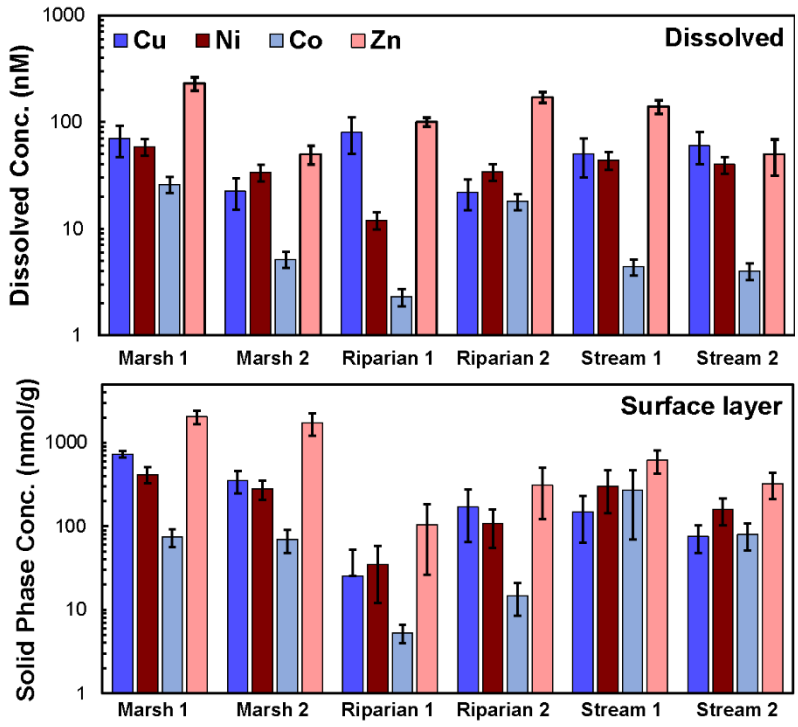

Figure 3. Dissolved (top) and total solid phase (bottom) trace metal concentrations for the study sites. The error bars for the dissolved concentrations are the uncertainties of individual analyses obtained from linear regression of the calibration curves. Error bars from the solid phase concentration reflect the calibration-derived uncertainties for samples from individual cores added in quadrature to the standard deviation of the mean values for the two duplicate cores collected at each site (Data tabulated in Tables S3 and S4).

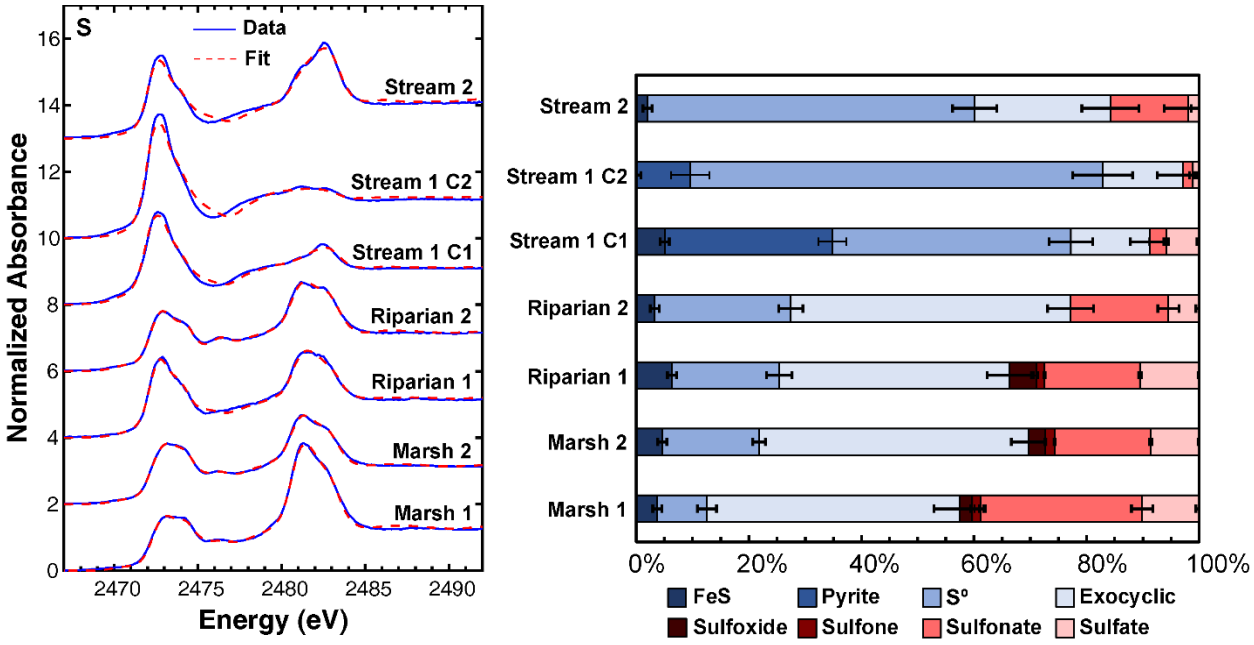

1335

1336 **Figure 4.** Sulfur K edge XANES spectra (solid) and fits (dashed) and the associated distribution

1337 of species for the surface layer soils and sediments at the study locations (Results tabulated in

1338 Table S12).

1339

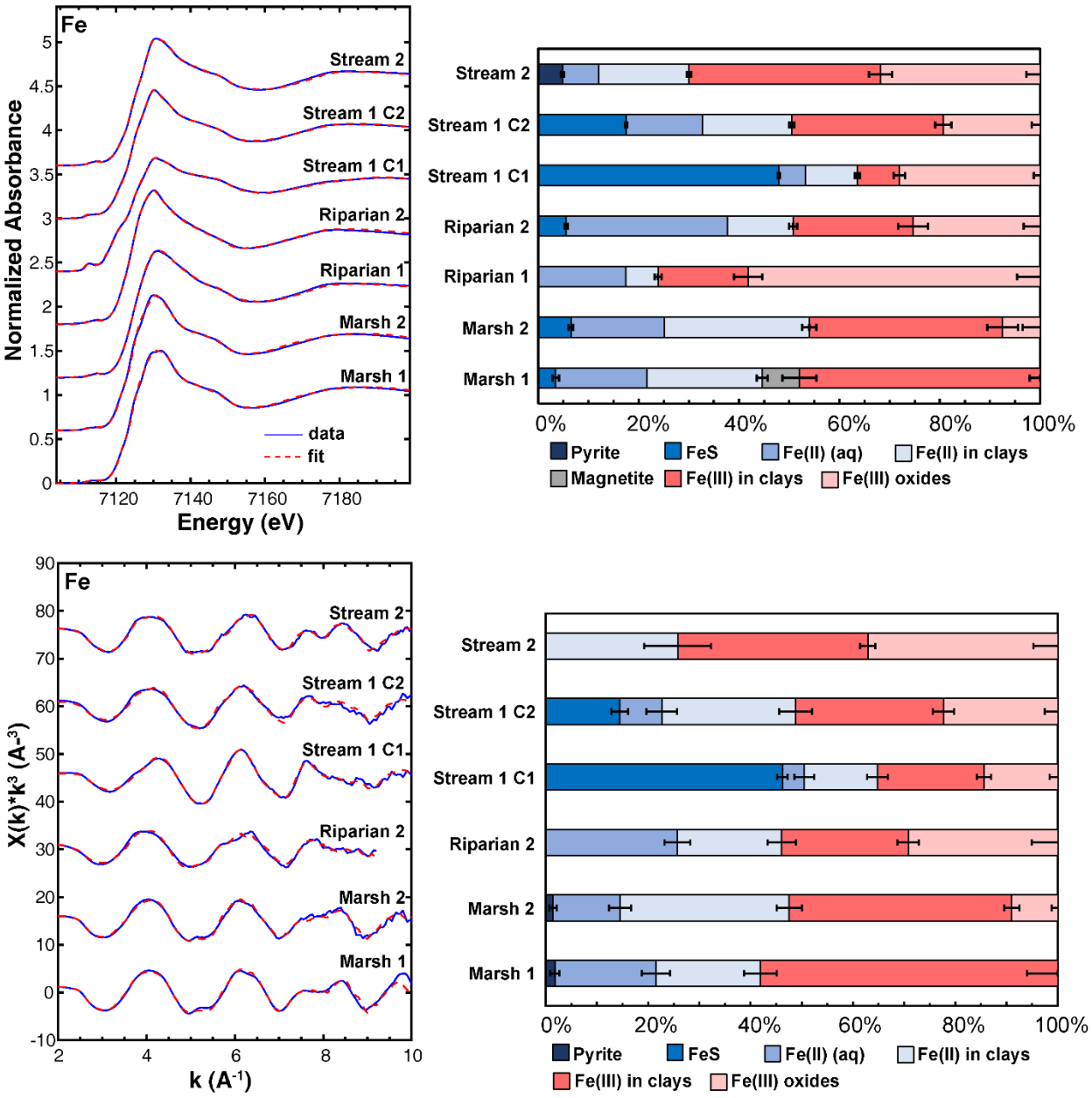

Figure 5. Iron K-edge XANES (top) and EXAFS (bottom) spectra (solid) and fits (dashed) and the associated distribution of species for the surface layer soils and sediments at the study locations. (Results tabulated in Tables S13 and S14)

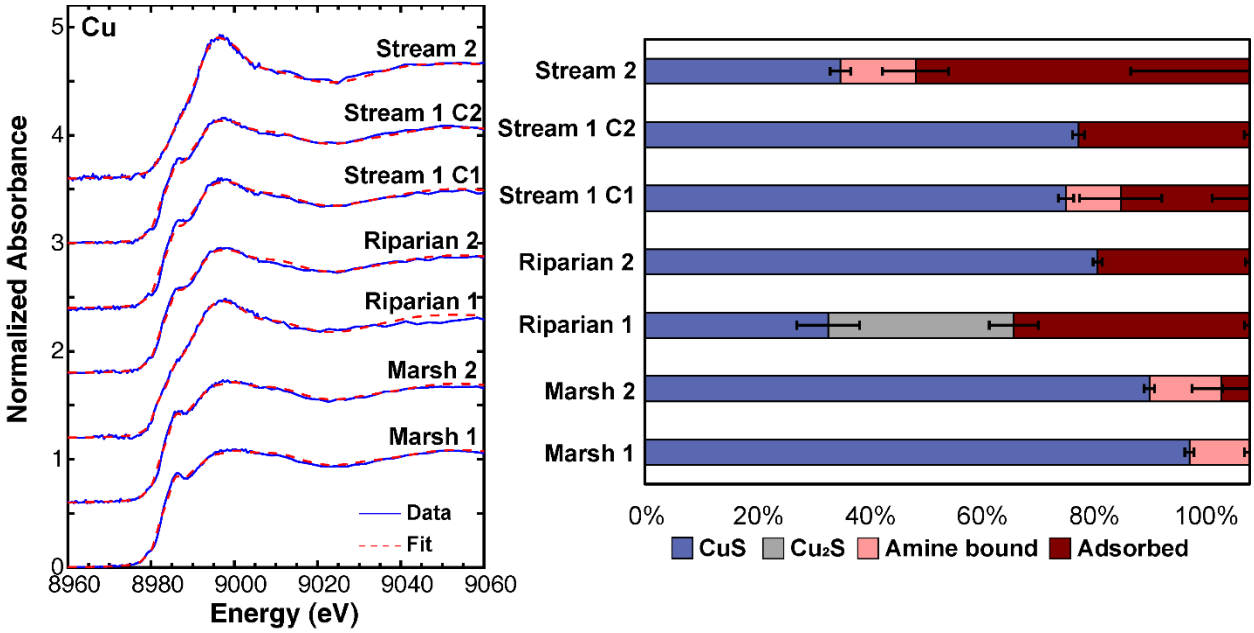

1347

1348 **Figure 6.** Cu-K edge XANES spectra (solid) and fits (dashed) and the associated distribution of

1349 species for the surface layer soils and sediments at the study locations (Results tabulated in Table

1350 S15).

1351

1352

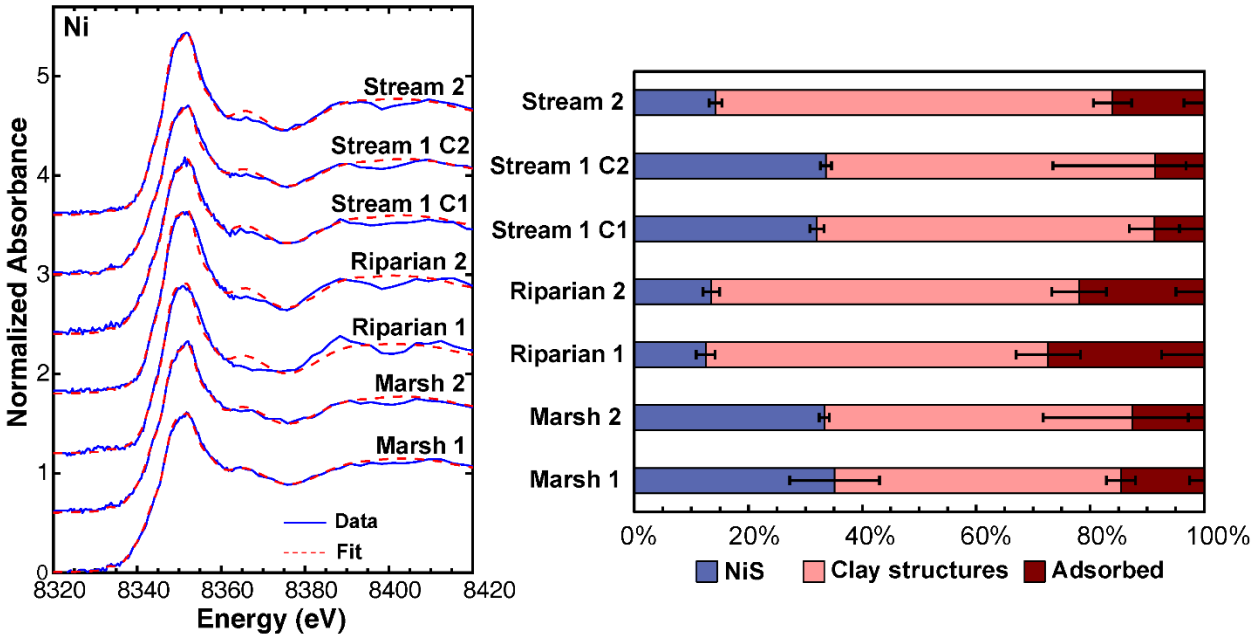

1353

1354 **Figure 7.** Ni-K edge XANES spectra (solid) and fits (dashed) and the associated distribution of

1355 species for the surface layer soils and sediments at the study locations (Results tabulated in Table

1356 S16).

1357

1358

1359

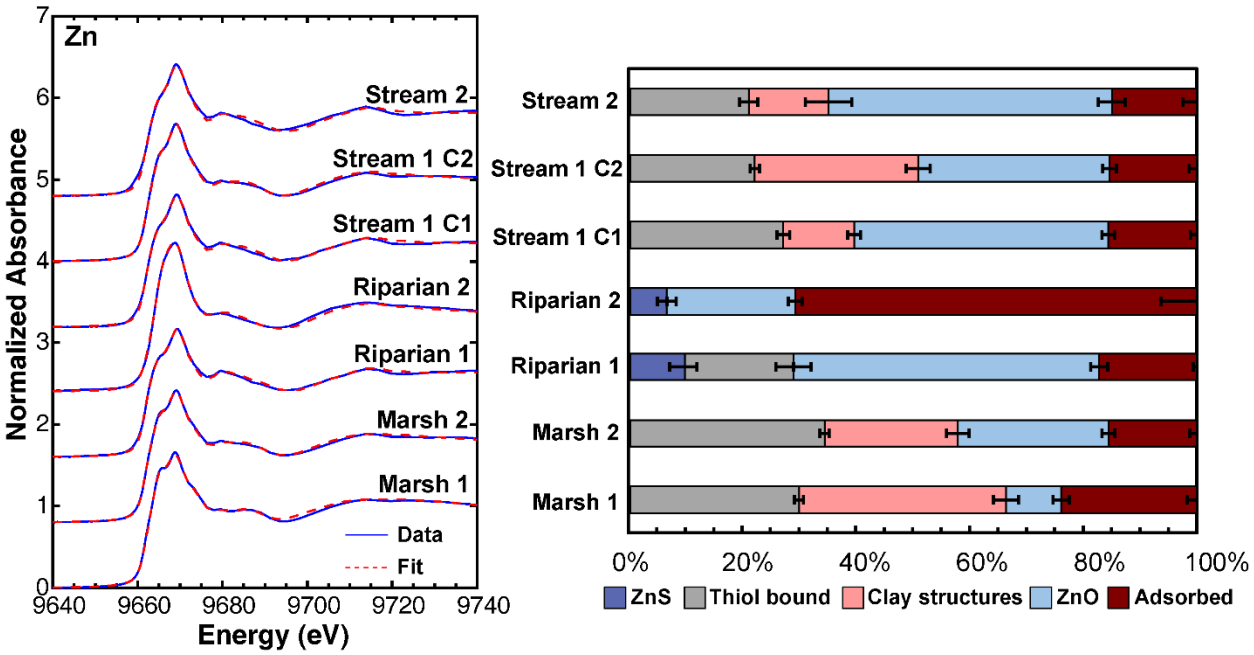

1360

1361 **Figure 8.** Zn-K edge XANES spectra (solid) and fits (dashed) and the associated distribution of

1362 species for the surface layer soils and sediments at the study locations (Results tabulated in Table

1363 S17).

1364

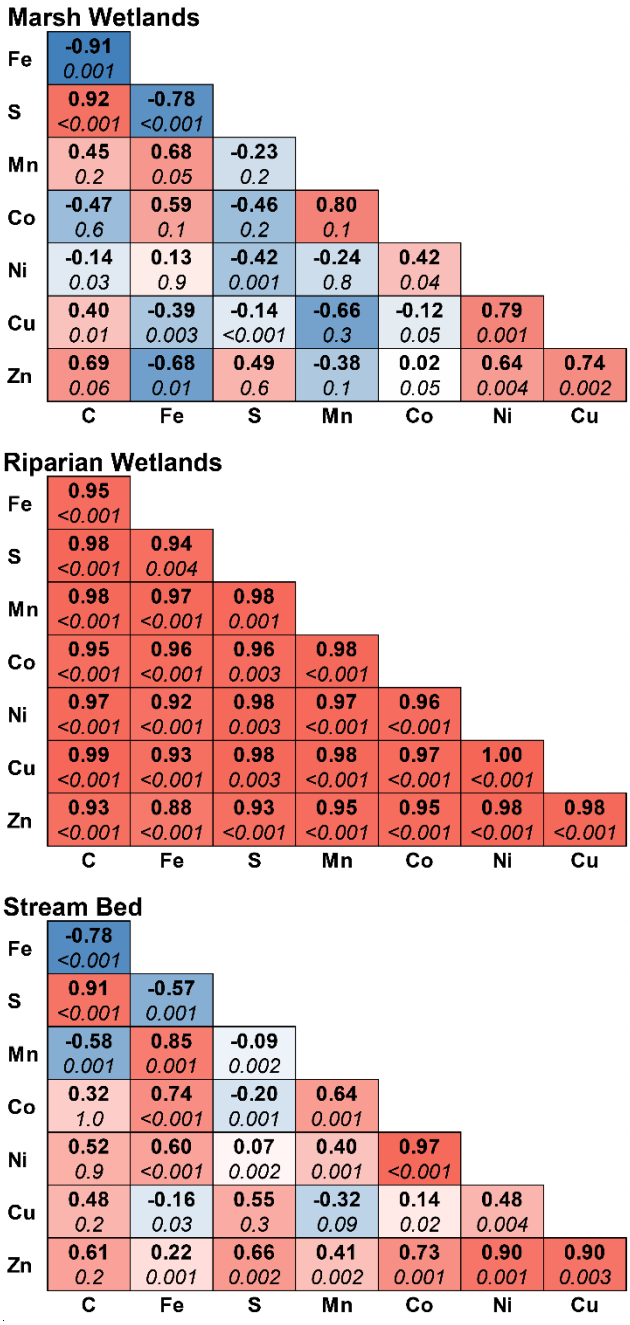

Figure 9. Correlation coefficients (R) and associated p-values derived from weighted linear regression of the solid-phase concentrations of each element pair. Data for the stream bed site excluded the single sample containing pyrite.

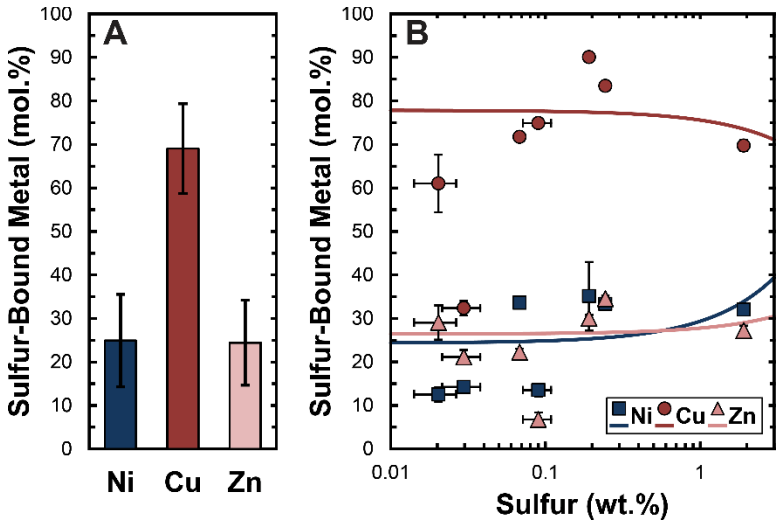

1370

1371 **Figure 10.** (A) Average and standard deviation of the fraction of trace metals bound to reduced

1372 sulfur as determined by XANES spectroscopy. (B) Variation in the fraction of each trace metal

1373 bound to reduced sulfur compared to the total sulfur content of the samples compared to trend

1374 lines for each metal (Cu: R = -0.06, p = 0.03; Ni: R = 0.37, p = 0.001; Zn: R = 0.18, p = 0.1)

1375 determined through linear regression weighted by the bivariate uncertainties.

1376

SUPPLEMENTARY MATERIAL FOR

Consistent Controls on Trace Metal Micronutrient Speciation in Wetland Soils and Stream Sediments

Jinshu Yan[1], Neha Sharma[2], Elaine D. Flynn[1], Daniel E. Giammar[2], Grace E. Schwartz[3†], Scott C. Brooks[3], Pamela Weisenhorn[4], Kenneth M. Kemner[4], Edward J. O'Loughlin[4], Daniel I. Kaplan[5], Jeffrey G. Catalano[1*]

1. Department of Earth and Planetary Sciences, Washington University, Saint Louis, MO, 63130, USA
2. Department of Energy, Environment, and Chemical Engineering, Washington University, Saint Louis, MO, 63130, USA
3. Oak Ridge National Laboratory, Oak Ridge, TN, 37830, USA
4. Argonne National Laboratory, Lemont, IL, 60439, USA
5. Savannah River National Laboratory, Aiken, SC, 29808, USA

*Corresponding author: catalano@wustl.edu
[†]Present address: Department of Chemistry, Wofford College, Spartanburg, SC 29303, USA

Synthesis of Reference Standards

Copper citrate was made using equal volumes (100 mL) of 0.15 M copper sulfate ($CuSO_4$) and 0.1 M sodium citrate. The solutions were heated to 100°C on a heated magnetic stir plate. The $CuSO_4$ solution was added to the citrate solution while continuously stirring in the fume hood. The mixture was stirred for 2 hours at 100°C then centrifuged at 4500 rpm for 5 minutes (Beckman Coulter SX4250 rotor) and the supernatant discarded. Copper citrate was washed three times with 50 mL of ultrapure water, centrifuged, and the supernatant discarded. It was then dried in a vacuum desiccator and ground with a mortar and pestle.

Zinc oxalate was prepared by mixing an equimolar ratio of zinc nitrate ($Zn(NO_3)_2$) and oxalic acid solutions as described by (Raj et al., 2011). While stirring, 10 mL of 1 M $Zn(NO_3)_2$ was added to 20 mL of 0.5 M oxalic acid. A milky white precipitate formed immediately. The solution was centrifuged at 4500 rpm for 10 minutes and the supernatant discarded. The precipitant was then rinsed three times with 50 mL of ultrapure water, centrifuged, and the supernatant discarded. Zinc oxalate was dried in a vacuum desiccator and then ground with a mortar and pestle.

To synthesize metal-cysteine, metal-histidine, and metal-glutathione complexes, solutions with a 1:10 ratio of metal to ligand were reacted based on published methods (Kelly et al., 2002; Beauchemin et al., 2004; Montargès-Pelletier et al., 2008; Dokken et al., 2009; Manceau et al., 2013; Van Der Ent et al., 2017). All solutions were prepared in the anaerobic chamber and using deoxygenated ultrapure water. Solutions containing 7 mM of copper chloride ($CuCl_2$), nickel chloride ($NiCl_2$), or zinc nitrate ($Zn(NO_3)_2$) and 70 mM of L-cysteine hydrochloride, L-histidine hydrochloride, or glutathione (reduced) were adjusted to pH 7 ± 0.2 using NaOH. The solutions containing the metal-ligand complexes were then removed from the anaerobic chamber and frozen. The samples were freeze-dried before being ground using a mortar and pestle.

Standards of Ni, Cu, and Zn adsorbed to goethite were also prepared. Goethite was synthesized using established methods (Schwertmann and Cornell, 2000). Briefly, 50 mL of 1 M iron nitrate ($Fe(NO_3)_3 \cdot 9H_2O$) was added to 90 mL of 5 M potassium hydroxide (KOH) over 1.5 min while continuously stirring. The solution was immediately diluted to 1 L using ultrapure water and heated at 70°C for 60 h. After cooling, the supernatant was discarded, and the goethite was rinsed three times with approximately 150 mL of ultrapure water through a vacuum filter. The goethite was stored as a suspension in ultrapure water and powder X-ray diffraction (XRD) was used to confirm that no other crystalline minerals precipitated. A solution of 0.01 M sodium chloride (NaCl), 0.001 M MOPS buffer, and 0.004 M $CuCl_2$, $NiCl_2$, or $Zn(NO_3)_2$ was reacted with 8 g/L goethite at pH 7.5. Samples were wrapped in Al foil to prevent photochemical reactions and rotated end-over-end for 24 h. They were then centrifuged at 4500 rpm and the supernatant decanted, filtered, acidified to 2% nitric acid, and analyzed via ICP-MS to confirm substantial adsorption had occurred.

Ni- and Zn-substituted trioctahedral Fe(II)-Mg smectite standards were synthesized by modifying the recipe for "Clay D" in Chemtob et al., (2015) to include 0.5 wt.% Ni or Zn, respectively, replacing an equivalent amount of Mg in the structure. Ni- and Fe(II)-substituted serpentines were prepared using a similar sol-gel procedure as used for the smectite standards. 18 mL of 0.5 M sodium metasilicate was added to 13 mL of a solution containing 1 M magnesium chloride and 0.003 M nickel chloride or iron(II) chloride. The resulting gels were aged overnight and then washed via centrifugation and decanting of the fluid, which was replaced with ultrapure water and centrifuged and decanted again. This process was repeated two additional times. The gels were then resuspended in ultrapure water and heated in a PTFE-lined hydrothermal vessel at 200°C for 14 days. After cooling the resulting solids were separated by vacuum filtration and dried

in a vacuum desiccator. XRD confirmed that poorly crystalline turbostratic lizardite was produced. Ni-substituted brucite was also prepared by mixing 20 mL of 1 M sodium hydroxide with 15 mL of 1 M magnesium chloride and 0.003 M nickel chloride. A white precipitate formed quickly and was aged overnight before washing via centrifugation and then drying in a vacuum desiccator. The formation of brucite was confirmed by XRD.

Ni- and Zn-substituted magnetite, as well as metal-free magnetite, were prepared by mixing stoichiometric amounts of iron(II) chloride and iron(III) chloride solutions. Nickel chloride and zinc chloride were added into the iron(III) chloride solution before mixing to yield an ~0.3 mol% substitution level for each metal; this step was not used in the metal-free magnetite synthesis. Sodium hydroxide was used to adjust the pH to 7.0±0.1 after fluid mixing, yielding a black precipitate. This suspension was continuously mixed overnight before being separated by vacuum filtration and then dried in a vacuum desiccator. All steps were performed in an anaerobic chamber. Magnetite was the sole product identified by XRD.

Goethite, hematite, lepidocrocite, and 2-line ferrihydrite were prepared following established procedures (Schwertmann and Cornell, 2000). The lepidocrocite was provided by Walter Schenkeveld. Mackinawite was prepared through direct precipitation in an anaerobic chamber following previously-described procedures (Swanner et al., 2019). Smectites from the Source Clay Repository were size fractionated and Na-saturated as previously described (Catalano and Brown, 2005). Preparation of all standards for data collection are described in the full manuscript.

Surface Water Composition

Major element concentrations and pH were similar among the two sampling locations at each of the field sites investigated (Table S1). While differences were observed between the three field sites, the overall water compositions were more distinct at the riparian wetlands compared to the marsh wetlands and the stream sediment sites. Surface waters in the riparian wetlands are dilute with sodium as the dominant cation (~280 μM) and pH values of 5.5 to 5.6. The marsh wetlands and stream system were more alkaline, having pH values of 7.5 to 8.1, with substantially higher calcium, magnesium, and sulfate concentrations. Sodium and chloride concentrations are higher in the stream system compared to the marsh wetlands, and the stream sites have the highest ionic strengths of the sites examined. Dissolved silica concentrations indicate that all fluids were supersaturated with respect to quartz but undersaturated with respect to amorphous silica.

Dissolved nutrient concentrations (Fig. S2; Table S5) varied substantially among the sites. Nitrate was greater than ammonium at all sampling locations except for location Riparian 2, where both were below detection limit. Notably, the stream sites had substantially elevated nitrate concentrations (160 to 210 μM) compared to the marsh and riparian wetland sites (<15 μM), because of contamination at the headwaters and wastewater treatment plant discharge. Dissolved phosphate concentrations were similar at the marsh and riparian wetlands, but the stream sites displayed slightly higher concentrations.

Alkalinity and dissolved organic carbon (DOC) were not measured at the time of sampling because of an oversight. Measurements of DOC on archived samples provide an upper bound on values in the original waters. Bicarbonate concentrations and pCO_2 were estimated using two approaches: (1) from dissolved inorganic carbon (DIC) measurements on archived samples and (2) via charge balance constraints. For the DIC-based estimation approach, the measured water

113 composition as well as the DIC and pH from the time of DIC measurement were input into a fully-
114 speciated geochemical model. The pH of most samples were greater than the field-measured values
115 because of CO_2 degassing. However, alkalinity is conserved during degassing. Field values of
116 bicarbonate and pCO_2 were thus determined by increasing the pCO_2 in the geochemical model
117 until the original, field-measured pH was obtained. For the charge-balance approach, measured
118 anion concentrations were inadequate to balance the cation charge, indicating a missing
119 bicarbonate component. This bicarbonate was added to the system in a geochemical model to reach
120 charge balance while maintaining the field-measured pH and other aspects of the fluid
121 composition. Both estimation approaches indicate that bicarbonate is the dominant anion in all
122 systems and yield similar pCO_2 values (Table S1).

123 The marsh wetlands host Ca-Mg-HCO_3 fluids, the stream sites Ca-HCO_3 fluids, and the
124 riparian wetlands Na-HCO_3 fluids. pCO_2 values were lowest in the marsh wetlands and highest in
125 the riparian wetlands, with all but one location sampled being elevated above equilibrium with the
126 atmospheric concentration. Filtered but non-acidified water samples returned to the laboratory
127 from the riparian wetland field sites had pH values of 7.2 to 7.3 immediately upon arrival and 7.7
128 after prolonger storage. This is consistent with a large pH increase associated with degassing of
129 fluids containing highly elevated pCO_2 values and suggesting that the estimated bicarbonate
130 concentrations are relatively accurate.

131

132 **Extractable Nutrients in the Soils and Sediments**

133 Extractable ammonium (Fig. S2) was substantially greater than extractable nitrate at all
134 sites, often by an order of magnitude, showing an opposite pattern of the surface waters. This is
135 consistent with ammonium retention via cation exchange but may also reflect denitrification. The

136 marsh soils contained the highest extractable ammonium concentrations and were the only soils
137 to show clear evidence for smectites in XRD (Fig. 1), suggesting that cation exchange was at
138 least partially responsible for the higher ammonium concentrations. Extractable phosphate was
139 highest in the marsh soils (Fig. S2), with concentrations obtained from location Stream 2 and
140 both riparian wetland sites an order of magnitude lower.
141
142 **Zinc Speciation in Cellulose Acetate Tape**
143 Cellulose acetate tape (e.g., Scotch^{TM} tape in the United States) is widely used for sample
144 mounting at synchrotron lightsources. It was noted during measurements at Advanced Photon
145 Source beamline 12-BM-B that the tape contained zinc based on its X-ray fluorescence spectrum.
146 A Zn K-edge XANES spectrum was collected in fluorescence yield from a stack of 10 layers of
147 tape. This is spectrally similar to the spectrum of zinc oxide (Fig. S9), indicating that this is the
148 dominant form of zinc in the tape.

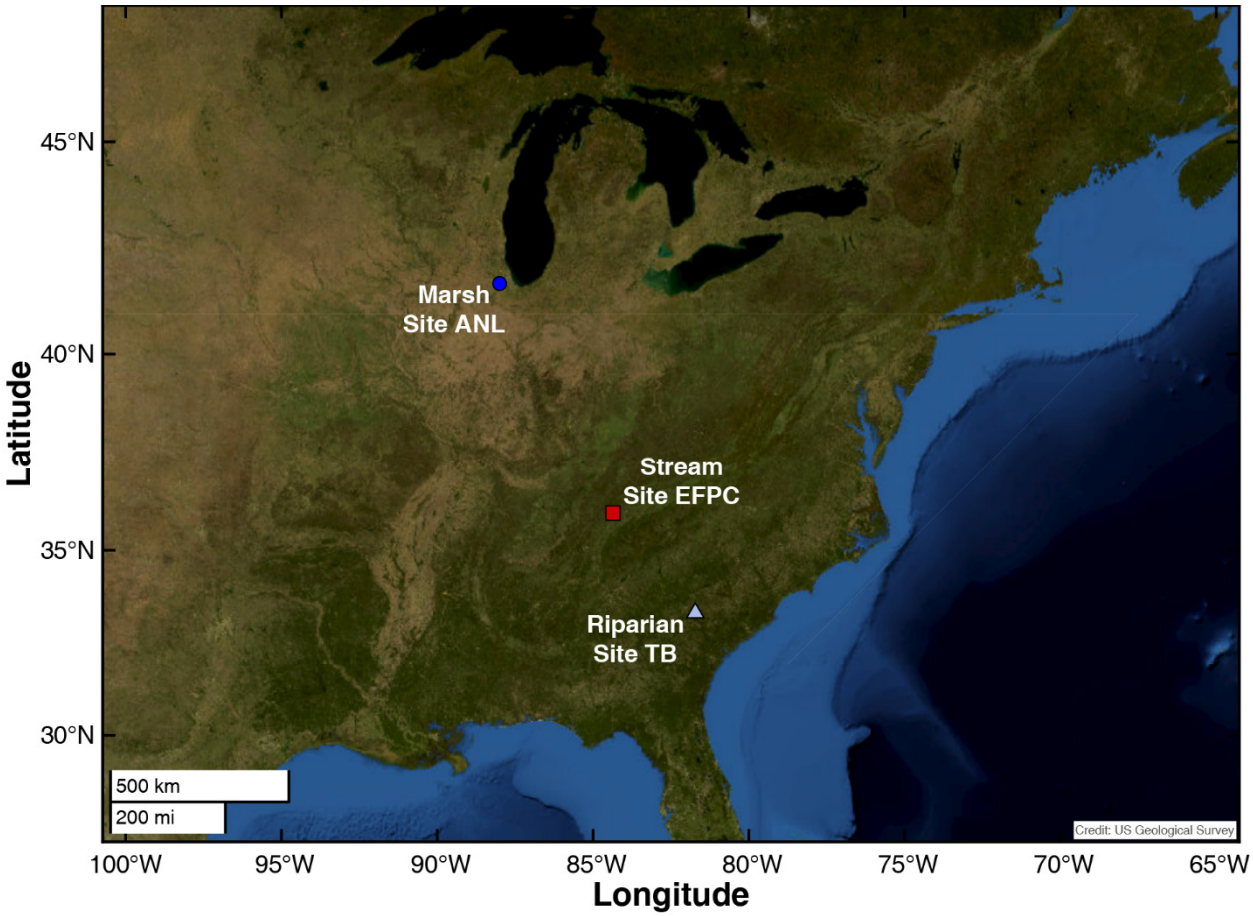

Figure S1. Location of the three field sites: Marsh wetlands at Argonne National Laboratory (Site ANL), stream bed sediments in the East Fork Poplar Creek (Site EFPC), and riparian wetlands in the Tims Branch watershed (Site TB). Details site descriptions and coordinates for these locations are provided in the Materials and Methods.

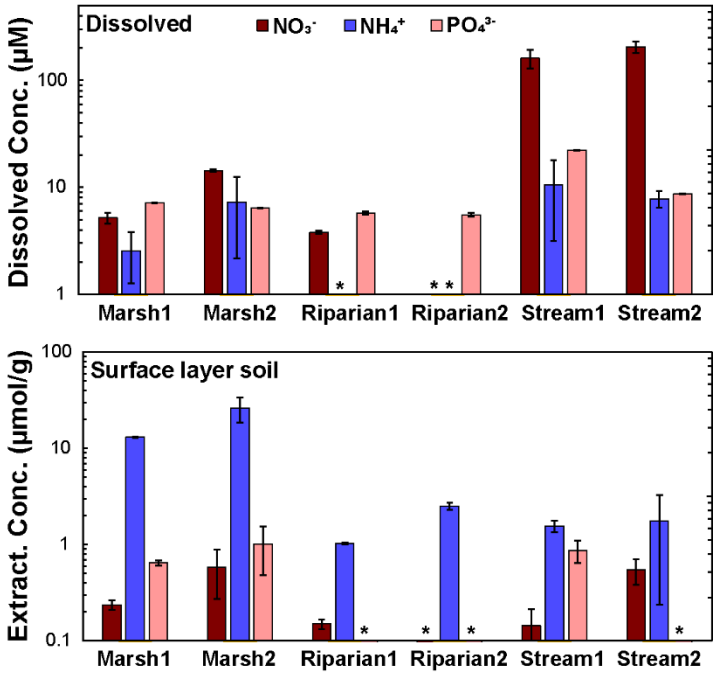

Figure S2. Dissolved (top) and solid-phase extractable (bottom) nitrate, ammonium, and phosphate concentrations for the study sites. Sample with an asterisk were below the ~2 µM or ~0.04 µmol/g detection limit.

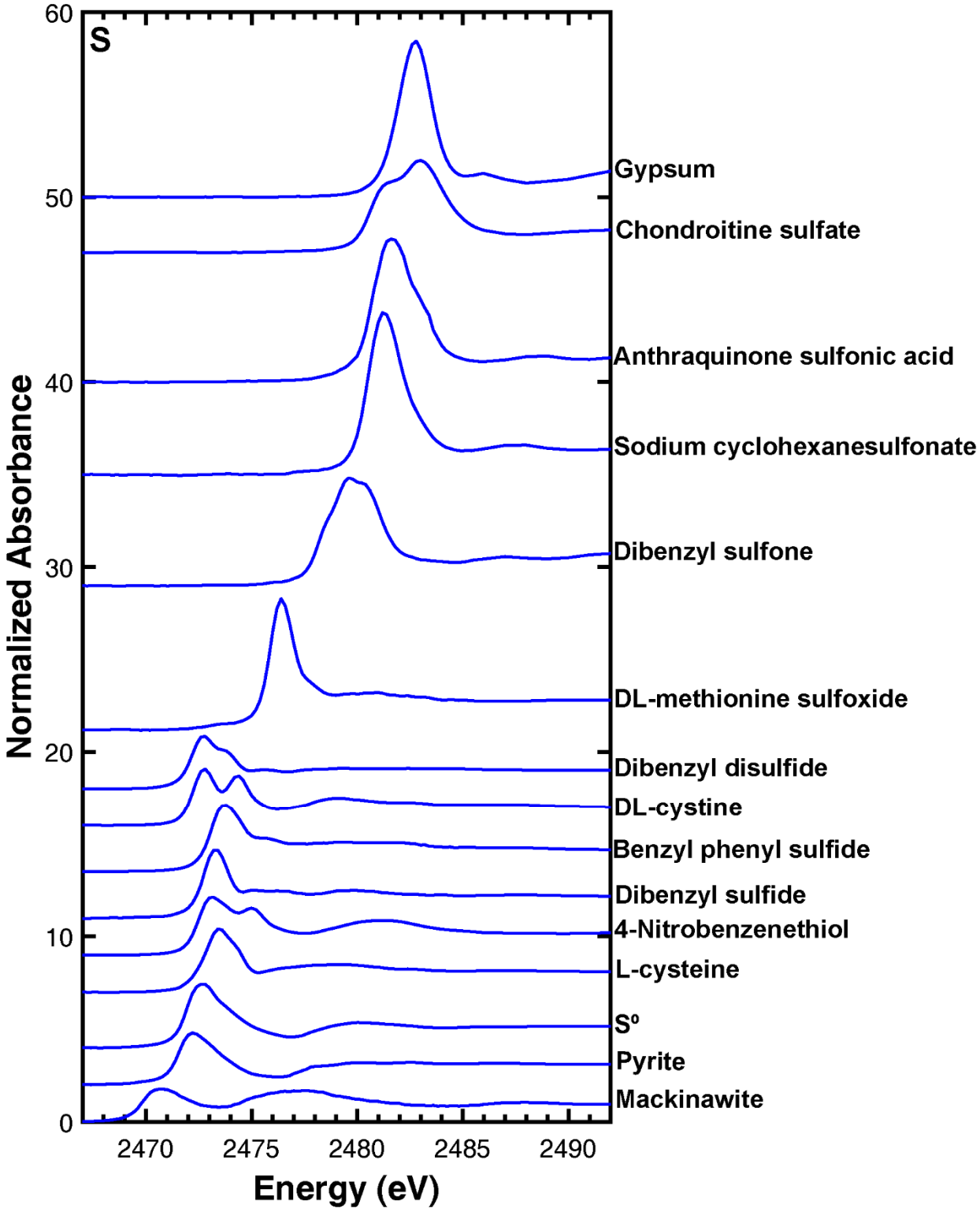

Figure S3. XANES spectra of sulfur reference standards. See Table S7 for more information.

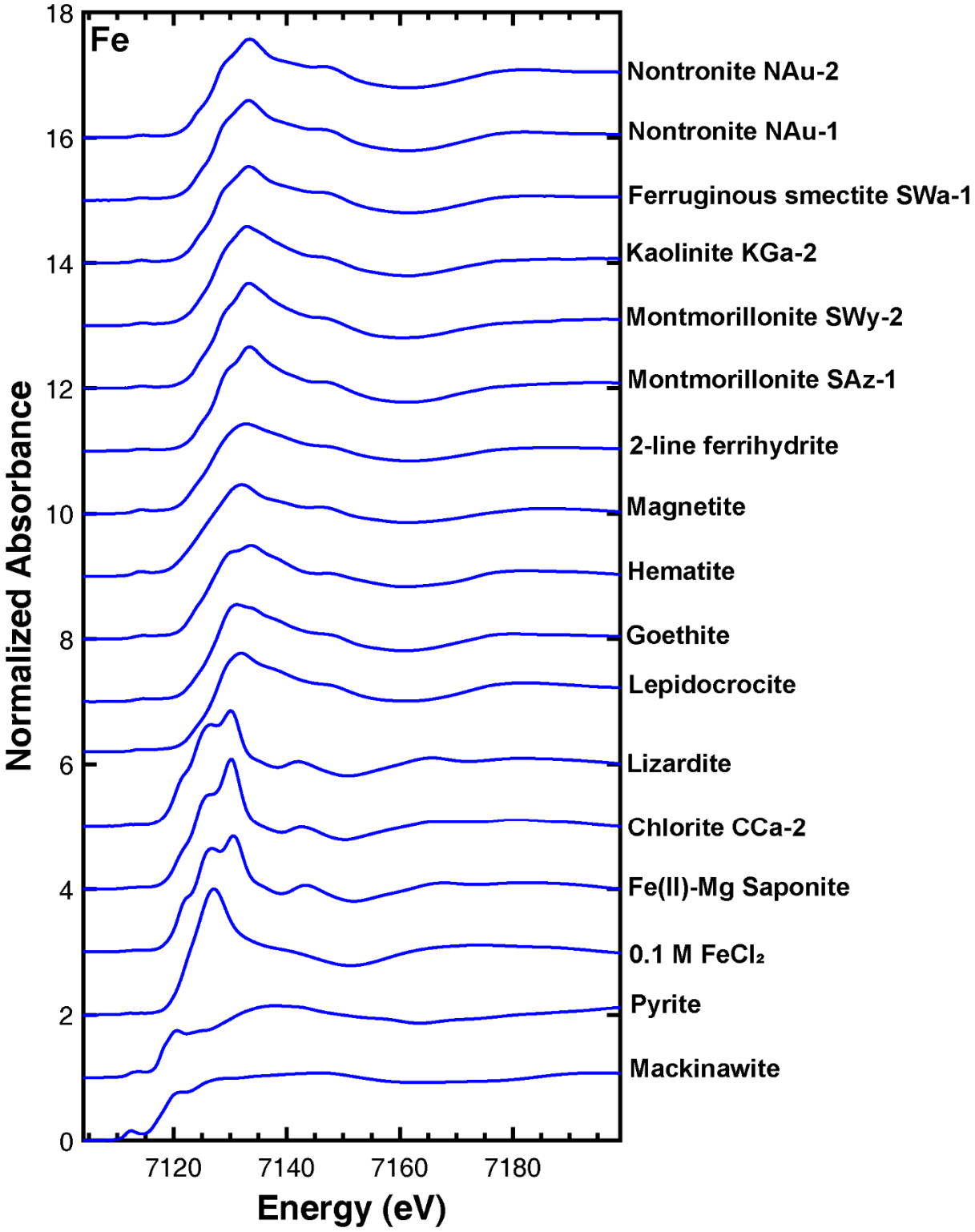

Figure S4. XANES spectra of iron reference standards. See Table S8 for more information.

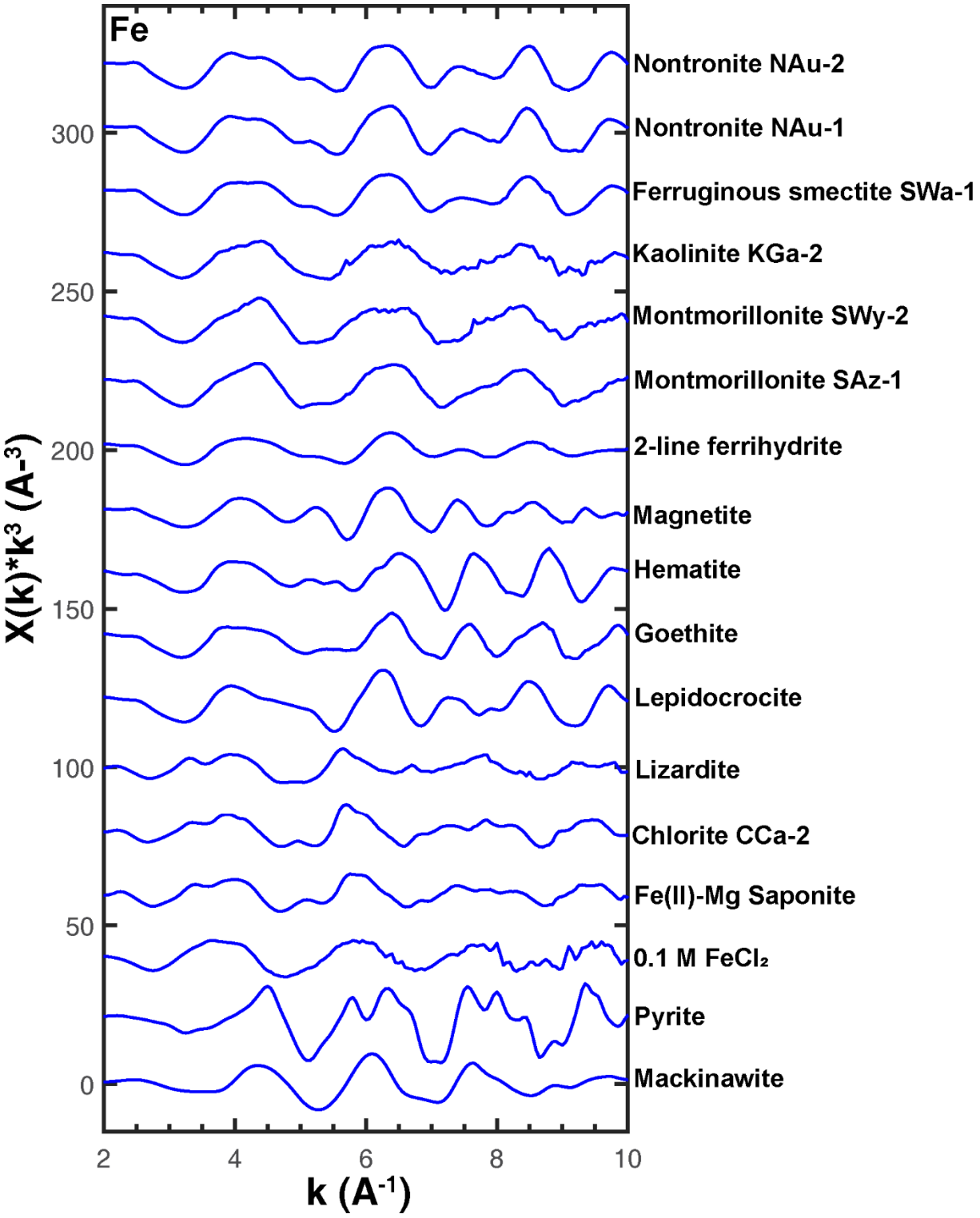

166

167 **Figure S5.** EXAFS spectra of iron reference standards. See Table S8 for more information.
168

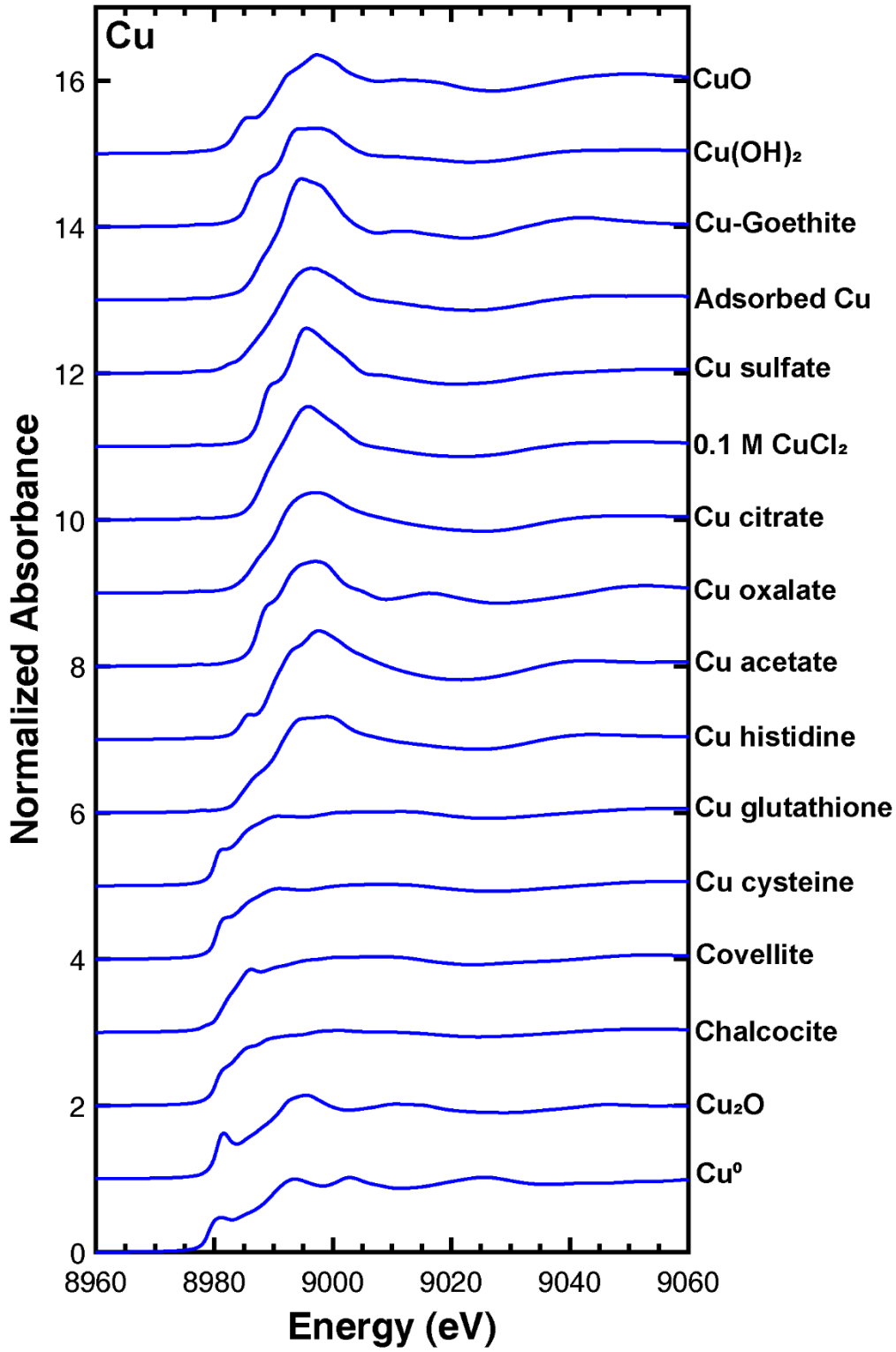

Figure S6. XANES spectra of copper reference standards. See Table S9 for more information.

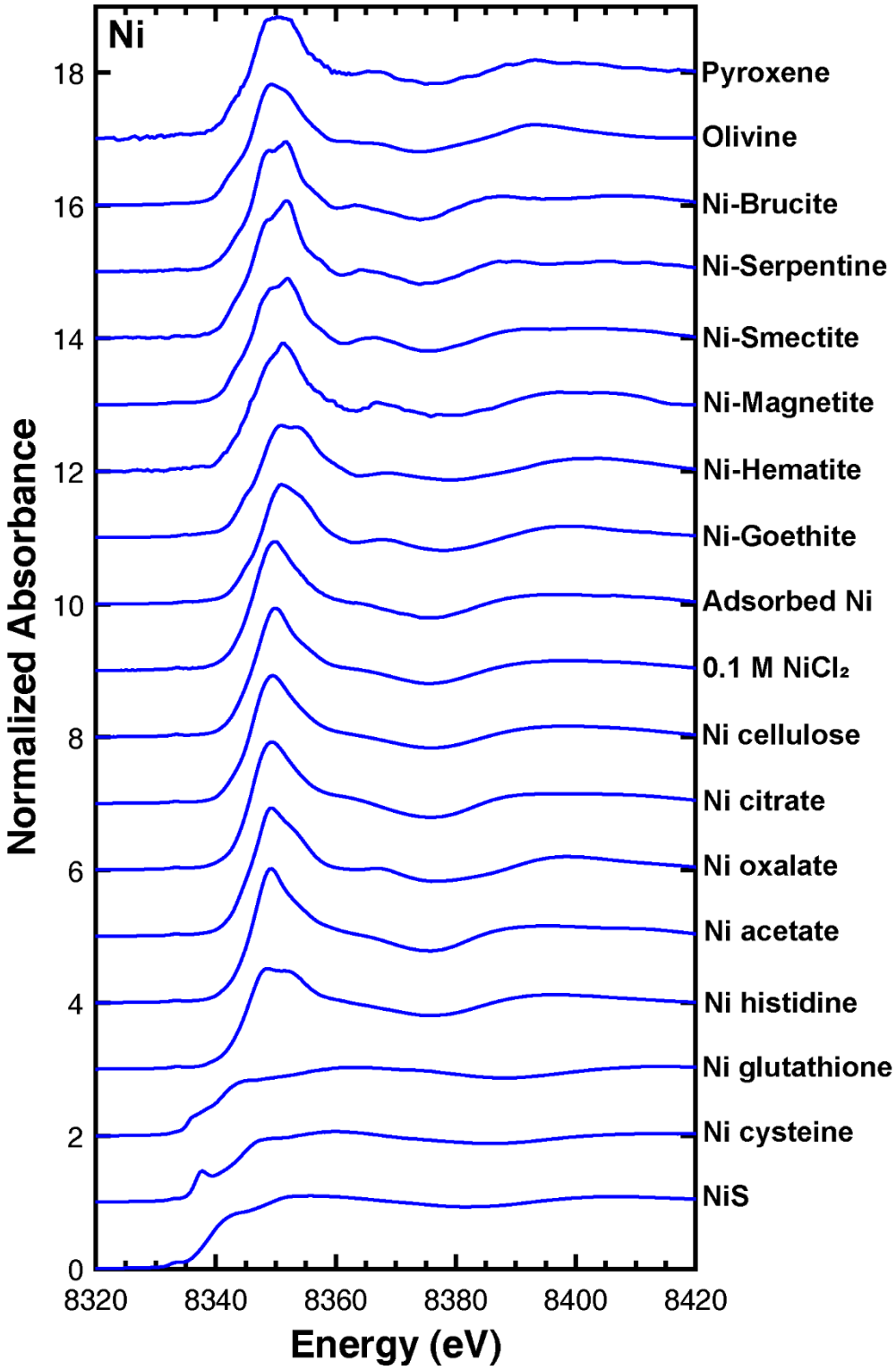

173

174 **Figure S7.** XANES spectra of nickel reference standards. See Table S10 for more information.
175

176

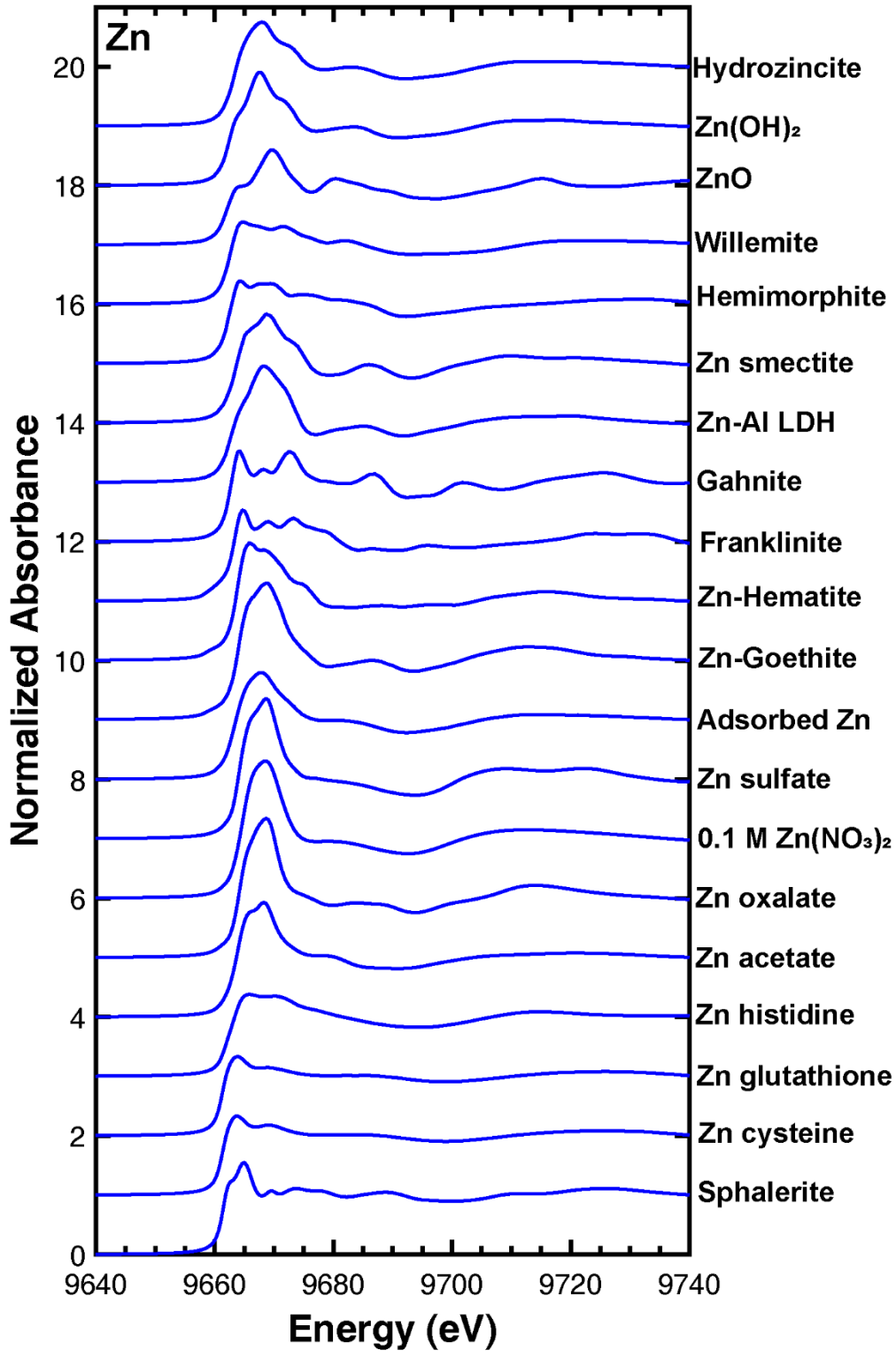

177

178 **Figure S8.** XANES spectra of zinc reference standards. See Table S11 for more information.
179

180

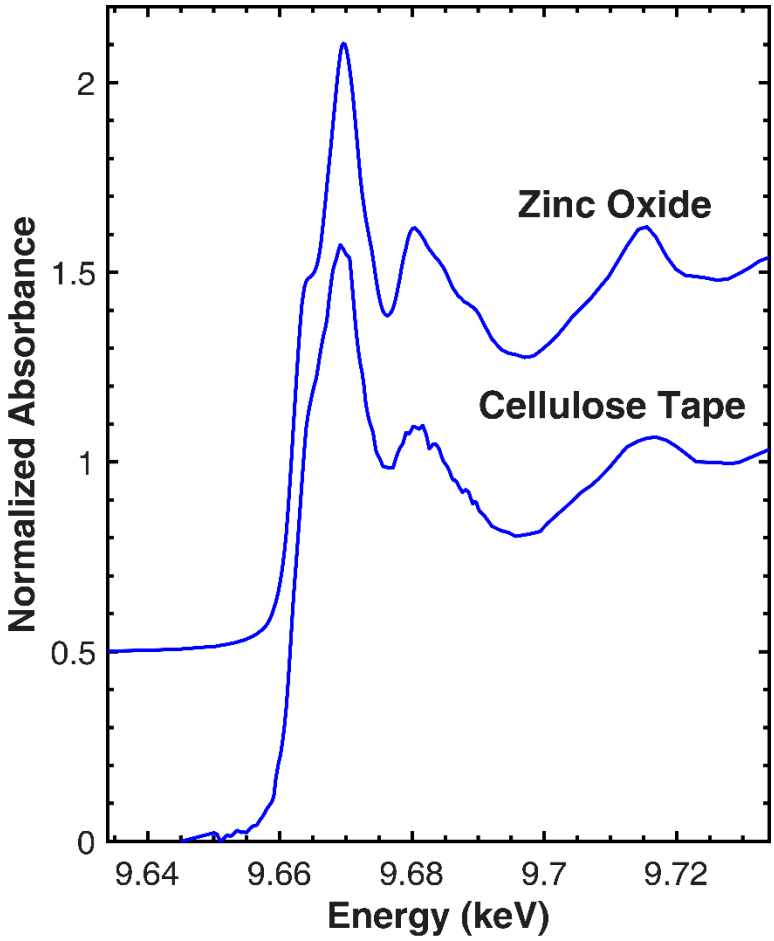

Figure S9. XANES spectrum of zinc in cellulose acetate tape compared to zinc oxide.

Table S1. Major elements and nutrients concentrations in surface waters.

Parameter	ANL 401	ANL 405	TBL	TBG	EFPC 5.4	EFPC 22-23
pH	8.10	7.62	5.58	5.49	7.51	7.60
T (°C)	4.2	4.7	13.8	14.2	12.3	14.2
Conductivity (µS)	220	371	n.a.[a]	n.a.	293	348
Ca (µM)	430±10	590±10	18±1	47±1	1280±30	1360±30
Mg (µM)	369±5	557±4	6.3±0.3	9.1±0.3	456±5	633±5
Na (µM)	70±10	220±10	296±2	258±3	670±20	800±10
K (µM)	13±2	22±2	0.8±0.1	0.8±0.2	12±1	9±3
Si (µM)	206±4	187±3	146.5±0.5	140.2±0.6	225±8	250±10
Al (µM)	-[b]	-	6.5±0.9	5.6±0.5	-	-
Fe (µM)	2.6±0.7	5±1	2.3±0.6	70±6	0.6±0.2	1.0±0.3
Mn (µM)	0.07±0.01	0.8±0.3	0.17±0.03	0.43±0.09	1.9±0.6	0.01±0.06
PO_4^{3-} (µM)	7.18±0.02	6.44±0.02	5.7±0.2	5.5±0.2	22.17±0.07	8.65±0.06
NO_3^- (µM)	5.2±0.6	14.4±0.4	3.8±0.1	-	160±30	210±30
NH_4^+ (µM)	3±1	7±5	-	-	11±7	8±1
SO_4^{2-} (µM)	410±30	332.5±0.8	10±1	13.6±0.04	217±3	396±4
F^- (µM)	2.26±0.06	3.7±0.4	1.9±0.1	1.28±0.07	14.6±0.3	22.4±0.6
Cl^- (µM)	68±4	221.8±0.4	61±2	77±1	465±5	578±7
Br^- (µM)	0.66±0.06	0.6±0.2	5±2	5±1	0.9±0.1	6.2±0.5
HCO_3^- (µM)[c]	776	1620	256	265	3100	3190
DIC_{calc} (µM[c]	801	1740	2050	2530	3350	3390
log pCO_2[c]	-3.56	-2.76	-1.44	-1.34	-2.33	-2.40
I (mM)[c]	2.8	3.9	0.38	0.44	6.0	6.9
DOC (mg C L^{-1})[d]	39.4	47.1	8.5	12.5	27.9	27.6
DIC (µM)[d]	790	2270	300	330	3920	4090
HCO_3^- (µM)[e]	764	2206	295	326	3877	4057
DIC_{calc} (µM)[e]	783	2369	2354	3110	4180	4304
log pCO_2[e]	-3.56	-2.62	-1.38	-1.25	-2.23	-2.29
I (mM)[e]	2.8	3.7	0.39	0.45	6.8	7.4
SI_{Quartz}	0.81	0.75	0.43	0.40	0.65	0.65
$SI_{Am.\ Silica}$	-0.66	-0.71	-0.95	-0.98	-0.75	-0.73

[a] Not measured. [b] Value below detection limit, 1.1 µM for Al, 2.1 µM for NO_3^-, 1.1 µM for NH_4^+. [c] Estimated values from charge balance; HCO_3^- concentration is sum of free and complexed species, with 0.1% to 1.6% occurring in complexes at all sites. [d] Measured on archived samples in May 2021. [e] Estimated values from DIC measurement after pCO_2 adjustment to match field pH; HCO_3^- concentration is sum of free and complexed species, with 0.1% to 1.6% occurring in complexes at all sites.

196 **Table S2.** Field blank major element and trace metal concentrations.
197

Conc.	ANL 401	ANL 405	EFPC 5.4	EFPC 22-23
Na (µM)	11.5±0.8	13±0.7	39±1	45±1
Al (µM)	-[a]	-	-	-
Si (µM)	-	-	-	-
Mg (µM)	-	-	-	-
K (µM)	-	-	-	-
Ca (µM)	-	-	-	-
Fe (µM)	0.3±0.1	0.3±0.1	n.a.[b]	n.a.
Mn (nM)	8±1	41±7	1.5±0.2	1.9±0.3
Co (nM)	1.7±0.3	3.7±0.7	1.5±0.3	1.6±0.3
Ni (nM)	7±1	134±24	2.4±0.5	2.7±0.5
Cu (nM)	15±5	22±7	7±2	8±3
Zn (nM)	19±3	16±2	7±1	11±1

198 [a] Below the limit of detection: Al =1.6 µM, Si=1.0 µM, Mg=0.51 µM, K=0.83 µM, Ca=4.7 µM.
199 [b] Not measured.

200 **Table S3.** Trace metal concentrations in surface water samples.

Sample	Cu (nM)	Ni (nM)	Co (nM)	Zn (nM)
ANL 401	70±20	60±10	26±5	230±30
ANL 405	20±7	34±6	5±1	50±10
TBL	80±30	12±2	2.3±0.4	100±10
TBG	22±7	34±6	18±3	170±20
EFPC 5.4	50±20	44±8	4.4±0.8	140±20
EFPC 22-23	60±20	40±7	4.0±0.7	50±20

201

202

203

204 **Table S4.** Trace metal concentrations in soils and sediments.

Sample	Cu (nmol/g)	Ni (nmol/g)	Co (nmol/g)	Zn (nmol/g)
Surface layer				
ANL 401	730±70	420±90	70±20	2100±400
ANL 405	400±100	280±70	70±20	1700±500
TBL	30±30	40±20	5±1	100±80
TBG	200±100	110±50	20±6	300±200
EFPC 5.4	150±80	300±200	300±200	600±200
EFPC 22-23	80±30	160±60	80±30	300±100
Second layer				
ANL 401	764±200	462±70	78±10	1833±300
ANL 405	366±100	377±100	102±40	1547±400
TBL	10±10	33±10	6±3	84±60
TBG	96±80	73±40	13±5	180±100
EFPC 5.4	84±60	184±90	95±40	483±300
EFPC 22-23	41±20	180±90	115±60	324±200

205

206

Table S5. KCl-extractable nutrients concentrations in the soils and sediments.

Sample	NO_3^- (µmol/g soil)	NH_4^+ (µmol/g soil)	PO_4^{3-} (µmol/g soil)
Surface layer			
ANL 401	0.24±0.03	13.0±0.2	0.64±0.04
ANL 405	0.6±0.3	26±8	1.0±0.5
TBL	0.15±0.02	1.03±0.02	0.057±0.001
TBG	0.01±0.01	2.5±0.2	0.06±0.04
EFPC 5.4	0.14±0.07	1.6±0.2	0.9±0.2
EFPC 22-23	0.5±0.2	2±2	0.036±0.006
Second layer			
ANL 401	0.245±0.009	4.9±0.3	0.35±0.02
ANL 405	0.3±0.1	5±2	0.45±0.05
TBL	0.10±0.03	0.21±0.02	0.01±0.03
TBG	0.02±0.03	1±1	0.022±0.008
EFPC 5.4	0.17±0.09	0.9±0.2	0.16±0.08
EFPC 22-23	0.6±0.5	2±1	0.030±0.007

Table S6. Major element content of the soils and sediment samples**.**

Sample	C (wt.%)	N (wt.%)	S (wt.%)	Fe (wt.%)	Mn (wt.%)
Surface layer					
ANL 401	8.7±0.4	0.79±0.02	0.18±0.01	2.3±0.3	0.011±0.003
ANL 405	11±2	1.0±0.2	0.28±0.04	2.2±0.3	0.014±0.005
TBL	1.1±0.3	0.3±0.1	0.018±0.009	0.20±0.08	0.0008±0.0005
TBG	4±2	0.05±0.02	0.07±0.03	1.8±0.8	0.003±0.001
EFPC 5.4	6±5	0.2±0.4	1.0±0.9	3±1	0.026±0.009
EFPC 22-23	0.42±0.09	0.05±0.07	0.02±0.01	2.4±0.2	0.04±0.01
Second layer					
ANL 401	6.45±0.02	0.65±0.02	0.100±0.002	2.5±0.3	0.009±0.001
ANL 405	3.24±0.05	0.337±0.009	0.068±0.003	3.0±0.1	0.020±0.006
TBL	0.19±0.03	0.017±0.002	0.014±0.008	0.19±0.08	- [a]
TBG	2.8±0.2	0.168±0.010	0.045±0.006	2.0±0.5	0.0023±0.0004
EFPC 5.4	2.14±0.03	0.160±0.004	0.065±0.005	1.4±0.2	0.016±0.006
EFPC 22-23	0.482±0.006	0.06±0.01	0.019±0.003	2.60±0.04	0.09±0.01

[a] Below detection limit.

213 **Table S7.** Sulfur K-edge XANES standards and sources.

Standard	Source/Reference
Mackinawite	Swanner et al. (2019)
Pyrite	Manceau and Nagy (2012)
Elemental S	Manceau and Nagy (2012)
L-cysteine	Manceau and Nagy (2012)
4-Nitrobenzenethiol	Manceau and Nagy (2012)
Dibenzyl sulfide	Manceau and Nagy (2012)
Benzyl phenyl sulfide	Manceau and Nagy (2012)
DL-cystine	Manceau and Nagy (2012)
Dibenzyl disulfide	Manceau and Nagy (2012)
DL-methionine sulfoxide	Manceau and Nagy (2012)
Dibenzyl sulfone	Manceau and Nagy (2012)
Sodium cyclohexanesulfonate	Manceau and Nagy (2012)
Anthraquinone sulfonic acid	Bohic et al. (2012)
Chondroitine sulfate	Cuif et al. (2003)
Gypsum	Manceau and Nagy (2012)

214 *Data were taken from the literature when a reference is given.
215

Table S8. Iron K-edge XANES standards and sources.

Standard	Source
Mackinawite	Synthesized
Pyrite	Ward's Science
0.1 M $FeCl_2$	Salt from Sigma-Aldrich
Fe(II)-Mg Saponite	Chemtob et al. (2015)
Chlorite CCa-2	Source Clay Repository, as received
Lizardite	Synthesized
Lepidocrocite	Synthesized
Goethite	Synthesized
Hematite	Synthesized
Magnetite	Synthesized
2-line Ferrihydrite	Synthesized
Montmorillonite SAz-1	Source Clay Repository, <2 μm
Montmorillonite SWy-2	Source Clay Repository, <2 μm
Kaolinite KGa-2	Source Clay Repository, as received
Ferruginous Smectite SWa-1	Source Clay Repository, <2 μm
Nontronite NAu-1	Source Clay Repository, <0.5 μm
Nontronite NAu-2	Source Clay Repository, <0.5 μm

*Synthesis methods of the reference standards are described in the section "Synthesis of Reference Standards". Data were taken from the literature when a reference is given.

220 **Table S9** Cu reference standards for EXAFS measurement and their sources.

Standard	Source/Reference
Copper(II) Acetate	Acros Organics
Copper(II) Oxalate	Alfa Aesar
Copper(II) Citrate	Synthesized
Copper(II) Sulfate	Fisher Scientific
Chalcocite (Cu_2S)	Alfa Aesar
Cu(II)-Cysteine Complex	Synthesized
Cu(II)-Histidine Complex	Synthesized
Cu(II)-Glutathione Complex	Synthesized
Covellite (CuS)	Butte, Montana, USA
Cu(II) adsorbed to goethite	Synthesized
Cu metal	EXAFS Materials
0.1 M $CuCl_2$	Salt from Sigma-Aldrich
Cu-substituted Goethite	Frierdich and Catalano (2012)
Copper(II) oxide	Frierdich and Catalano (2012)
Copper(I) oxide	Frierdich and Catalano (2012)
Copper(II) hydroxide	Alfa Aesar; See Frierdich and Catalano (2012) for data collection information.

221 *Synthesis methods of the reference standards are described in the section "Synthesis of
222 Reference Standards". Data were taken from the literature when a reference is given.
223

Table S10. Ni reference standards for EXAFS measurement and their sources.

Standard	Source/Reference
Nickel(II) Acetate	Acros Organics
Nickel(II) Oxalate	Alfa Aesar
Nickel(II) Citrate	Alfa Aesar
Nickel(II) Sulfide	Alfa Aesar
Ni(II)-Cysteine Complex	Synthesized
Ni(II)-Histidine Complex	Synthesized
Ni(II)-Glutathione Complex	Synthesized
Ni(II)-Cellulose Complex	Synthesized
Ni-substituted Hematite	Frierdich et al. (2011)
Ni-substituted Goethite	Frierdich et al. (2011)
Ni-substituted Magnetite	Synthesized
Pyroxene (Augite)	Ontario, Canada
Olivine	San Carlos, Arizona, USA
Ni-substituted Brucite	Synthetized
Ni-substituted Serpentine	Synthetized
Ni-substituted Fe(II)-Mg Trioctahedral Smectite	Synthetized
Ni(II) adsorbed to goethite	Synthetized
0.1 M $NiCl_2$	Salt from Sigma-Aldrich

*Synthesis methods of the reference standards are described in the section "Synthesis of Reference Standards". Data were taken from the literature when a reference is given.

Table S11. Zn reference standards for EXAFS measurement and their sources.

Standard	Source/Reference
Zinc(II) Acetate	Fisher Scientific
Zinc(II) Oxalate	Synthesized
0.1 M $Zn(NO_3)_2$	Salt from J.T. Baker
Zinc(II) Sulfate	Fisher Scientific
Zn(II)-Cysteine Complex	Synthesized
Zn(II)-Histidine Complex	Synthesized
Zn(II)-Glutathione Complex	Synthesized
Franklinite	Luo et al. (2011)
Gahnite	Luo et al. (2011)
Willemite	Luo et al. (2011)
Hemimorphite	Luo et al. (2011)
Zinc(II) Hydroxide	Luo et al. (2011)
Zn-Al layered double hydroxide	Luo et al. (2011)
Zn smectite	Synthesized
Zinc(II) Oxide	Luo et al. (2011)
Hydrozincite	Luo et al. (2011)
Sphalerite	Pettus County, Missouri, USA
Zn-substituted Hematite	Frierdich and Catalano (2012a)
Zn-substituted Goethite	Frierdich and Catalano (2012a)
Zn adsorbed to goethite	Synthesized

*Synthesis methods of the reference standards are described in the section "Synthesis of Reference Standards". Data were taken from the literature when a reference is given.

Table S12. Sulfur XANES linear combination fitting results.

Standard	Marsh 1	Marsh 2	Riparian 1	Riparian 2	Stream 1 C1	Stream 1 C2	Stream 2
Fitting Components							
Gypsum	10.1±0.6%	8.6±0.2	5.5±0.6%	10.5±0.2%	5.8±0.4%	1.1±0.7%	16±1%
Anthraquinone sulfonic acid	6±2%	- [a]	9±2%	-	3.0±0.4%	1.7±0.6%	7±3%
Sodium cyclohexanesulfonate	23±1%	17.1±0.2	9±1%	17.0±0.2	-	-	5±2%
Dibenzyl sulfone	1.6±0.4%	1.6±0.2%	-	1.5±0.2	-	-	-
DL-methionine sulfoxide	2.2±0.4%	3.0±0.2%	-	4.8±0.4%	-	-	-
Dibenzyl disulfide	-	-	35±4%	5±4%	14±3%	14±5%	21±4%
Cystine	17±2%	16±1%	6±2%	18±1%	-	-	-
Benzyl phenyl sulfide	10±3%	13±2%	-	-	-	-	-
4-Nitrobenzenethiol	10±2%	7±1%	-	-	-	-	-
Cysteine	8±3%	13±2%	8±1%	18±1%	-	-	-
Elemental S	9±2%	17±1%	24±2%	19±2%	42±4%	73±5%	50±3%
Pyrite	-	-	-	-	30±3%	10±3%	-
Mackinawite	3.7±0.8%	4.6±0.5%	3.3±0.7%	6.4±0.6%	5±1%	-	2±1%
Component sum	1.075	0.977	1.063	1.006	1.009	1.093	1.006
R factor	0.003	0.002	0.005	0.003	0.01	0.02	0.02
χ_v^2	0.002	0.0009	0.003	0.001	0.004	0.01	0.008
Groupings							
FeS	3.7±0.8%	4.6±0.5%	3.3±0.7%	6.4±0.6%	5±1%	-	2±1%
Pyrite	-	-	-	-	30±3%	10±3%	-
S^0	9±2%	17±1%	24±2%	19±2%	42±4%	73±5%	50±3%
Exocyclic	45±5%	48±3%	50±4%	41±4%	14±3%	14±5%	21±4%
Sulfoxide	2.2±0.4%	3.0±0.2%	-	4.8±0.4%	-	-	-
Sulfone	1.6±0.4%	1.6±0.2%	-	1.5±0.2%	-	-	-
Sulfonate	29±2%	17.1±0.2%	17±2%	17.0±0.2%	3.0±0.4%	2±1%	12±4%
Sulfate (inorganic)	10.1±0.6	8.6±0.2%	5.5±0.6%	10.5±0.2%	5.8±0.4%	1±1%	16±1%

[a] Not present in final fit.

Table S13. Iron XANES linear combination fitting results.

Standard	Marsh 1	Marsh 2	Riparian 1	Riparian 2	Stream 1 C1	Stream 1 C2	Stream 2
Fitting Components							
Pyrite	-	-	-	-	-	-	4.8±0.3%
FeS	3.5±0.7%	6.5±0.5%	-	5.6±0.3%	48.0±0.2%	17.5±0.2%	-
Fe(II) (aq)	18.2±0.7%	19±1%	17.5±0.4%	32.1±0.4%	5.3±0.3%	15.2±0.3%	7.2±0.3%
Fe(II)-Mg Smectite	23±1%	29±1%	-	-	10.3%±0.5%	-	-
Chlorite	-	-	6.4±0.7%	13.1±0.8%	-	17.7±0.5%	18.0±0.4%
Magnetite	7%±3%	-	-	-	-	-	-
Montmorillonite	48±2%	39±3%	-	-	8±1%	-	-
Ferruginous smectite	-	-	-	-	-	30±2%	38±2%
Kaolinite	-	-	18±3%	24±3%	-	-	-
Lepidocrocite	-	7±4%	-	-	-	-	-
Goethite	-	-	11±3%	25±3%	28±1%	19±2%	-
2-line ferrihydrite	-	-	48±2%	-	-	-	32±3%
Component sum	1.01	1.015	0.996	1.006	0.999	1.004	0.996
R factor	0.0004	0.0006	0.0001	0.0002	0.0001	0.00008	0.0001
χ_v^2	0.0001	0.0002	0.00004	0.00005	0.00002	0.00002	0.00004
Groupings							
Pyrite	-	-	-	-	-	-	4.8±0.3%
FeS	3.5±0.7%	6.5±0.5%	-	5.6±0.3%	48.0±0.2%	17.5±0.2%	-
Fe(II) (aq)	18.2±0.7%	19±1%	17.5±0.4%	32.1±0.4%	5.3±0.3%	15.2±0.3%	7.2±0.3%
Fe(II) in clays	23±1%	29±1%	6.4±0.7%	13.1±0.8%	10.3±0.5%	17.7±0.5%	18.0±0.4%
Magnetite	7±3%	-	-	-	-	-	-
Fe(III) in clays	48±2%	39±3%	18±3%	24±3%	8±1%	30±2%	38±2%
Fe(III) oxides	-	7±4%	58±5%	25±3%	28±1%	19±2%	32±3%

[a] Not present in final fit.

Table S14. Iron EXAFS linear combination fitting results.

Standard	Marsh 1	Marsh 2	Riparian 2	Stream 1 C1	Stream 1 C2	Stream 2
Fitting Components						
Pyrite	1.8±0.9%	1.4±0.8%	-	-	-	-
FeS	-	-	-	46±1%	14±2%	-
Fe(II) (aq)	20±3%	13±2%	26±3%	4±2%	8±3%	-
Fe(II)-Mg Smectite	20±3%	33±2%	-	-	-	6±3%
Chlorite	-	-	20±3%	14±2%	26±3%	19±3%
Montmorillonite	24±3%	43±2%	25±2%	21±1%	29±2%	37±2%
Ferruginous smectite	34±3%	-	-	-	-	-
Lepidocrocite	-	9±1%	-	-	-	-
Goethite	-	-	-	14±2%	22±3%	27±2%
2-line ferrihydrite	-	-	13±4%	-	-	10±3%
Hematite	-	-	16±1%	-	-	-
Component sum	1.008	0.932	0.904	0.889	0.886	0.861
R factor	0.04	0.03	0.04	0.02	0.05	0.02
χ_v^2	0.3	0.2	0.2	0.1	0.3	0.1
Groupings						
Pyrite	1.8±0.9%	1.4±0.8%	-	-	-	-
FeS	-	-	-	46±1%	14±2%	-
Fe(II) (aq)	20±3%	13±2%	26±3%	4±2%	8±3%	-
Fe(II) in clays	20±3%	33±2%	20±3%	14±2%	26±3%	26±7%
Fe(III) in clays	58±6%	43±2%	25±2%	21±1%	29±2%	37±2%
Fe(III) oxides	-	9±1%	29±5%	14±2%	22±3%	37±5%

[a] Not present in final fit.

Table S15. Copper XANES linear combination fitting results.

Standard	Marsh 1	Marsh 2	Riparian 1	Riparian 2	Stream 1 C1	Stream 1 C2	Stream 2
Fitting Components							
Covellite	90±1%	83±1%	40±4%	75±1%	70±1%	72±1%	32±2%
Chalcocite	- [a]	-	30±4%	-	-	-	-
Cu(II)-Histidine	10±1%	12±5%	-	-	9±7%	-	13±5%
0.1 M $CuCl_2$	-	-	-	-	-	-	21±8%
Ads. Cu	-	5±4%	40±1%	25±1%	21±6%	28±1%	34±8%
Component sum	1.028	1.04	1.081	1.028	1.041	1.012	1.004
R factor	0.002	0.002	0.003	0.002	0.003	0.002	0.001
χ_v^2	0.0003	0.0004	0.0007	0.0004	0.0007	0.0005	0.0003
Groupings							
CuS	90±1%	83±1%	40±4%	75±1%	70±1%	72±1%	32±2%
Cu_2S	-	-	30±4%	-	-	-	-
Amine bound	10±1%	12±5%	-	-	9±7%	-	13±5%
Adsorbed	-	5±4%	40±1%	25±1%	21±6%	28±1%	55±20%

[a] Not present in final fit.

Table S16. Nickel XANES linear combination fitting results.

Standard	Marsh 1	Marsh 2	Riparian 1	Riparian 2	Stream 1 C1	Stream 1 C2	Stream 2
Fitting Components							
NiS	35±8%	33±1%	13±2%	14±1%	32±1%	34±1%	14±1%
Ni-Smectite	50±3%	45±8%	60±6%	65±5%	59±4%	45±9%	70±3%
Serpentine	-[a]	9±8%	-	-	-	13±9%	-
0.1 M $NiCl_2$	15±3%	13±3%	27±7%	22±5%	-	-	16±4%
Ads. Ni	-	-	-	-	9±4%	9±3%	-
Component sum	1.014	1.03	0.974	1.028	1.074	1.024	1.011
R factor	0.002	0.002	0.007	0.005	0.005	0.003	0.003
χ_v^2	0.0005	0.0007	0.002	0.002	0.001	0.0009	0.001
Groupings							
NiS	35±8%	33±8%	13±2%	13±1%	32±1%	34±1%	14±1%
Clay structures	50±3%	54±3%	60±6%	65±5%	59±4%	58±18%	70±3%
Adsorbed	15±3%	12±3%	27±7%	22±5%	9±4%	9±3%	16±4%

[a] Not present in final fit.

Table S17. Zinc XANES linear combination fitting results.

Standard	Marsh 1	Marsh 2	Riparian 1	Riparian 2	Stream 1 C1	Stream 1 C2	Stream 2
Fitting Components							
Zn-Smectite	36±2%	23±2%	- [a]	-	12±1%	29±2%	14±4%
ZnO	10±1%	27±1%	54±2%	23±1%	45±1%	34±1%	50±2%
Zn cysteine	30±1%	-	-	-	27±1%	22±1%	-
Zn glutathione	-	34±1%	19±3%	-	-	-	21±2%
Sphalerite	-	-	10±2%	7±2%	-	-	-
Zn Acetate	24±2%	-	-	-	-	-	-
$ZnSO_4$	-	16±1%	17±1%	-	16±1%	15±1%	15±2%
Zn Nitrate	-	-	-	41±2%	-	-	-
Ads. Zn	-	-	-	29±4%	-	-	-
Component sum	1.006	0.996	0.995	0.977	0.996	0.999	0.984
R factor	0.0004	0.0003	0.0004	0.0005	0.0007	0.0004	0.001
χ_v^2	0.02	0.0001	0.0002	0.0002	0.01	0.0001	0.05
Groupings							
ZnS	-	-	10±2%	7±2%	-	-	-
Thiol bound	30±1%	34±1%	19±3%	-	27±1%	22±1%	21±2%
Clay structures	36±2%	23±2%	- [a]	-	12±1%	29±2%	14±4%
ZnO	10±1%	27±1%	54±2%	23±1%	45±1%	34±1%	50±2%
Adsorbed	24±2%	16±1%	17±1%	70±6%	16±1%	15±1%	15±2%

[a] Not present in final fit.

REFERENCES

Beauchemin S., Hesterberg D., Nadeau J. and McGeer J. C. (2004) Speciation of hepatic Zn in trout exposed to elevated waterborne Zn using X-ray absorption spectroscopy. *Environ. Sci. Technol.* **38**, 1288–1295.

Bohic S., Cotte M., Salomé M., Fayard B., Kuehbacher M., Cloetens P., Martinez-Criado G., Tucoulou R. and Susini J. (2012) Biomedical applications of the ESRF synchrotron-based microspectroscopy platform. *J. Struct. Biol.* **177**, 248–258.

Catalano J. G. and Brown G. E., Jr. (2005) Uranyl adsorption onto montmorillonite: Evaluation of binding sites and carbonate complexation. *Geochim. Cosmochim. Acta* **69**, 2995–3005.

Chemtob S. M., Nickerson R. D., Morris R. V., Agresti D. G. and Catalano J. G. (2015) Synthesis and structural characterization of ferrous trioctahedral smectites: Implications for clay mineral genesis and detectability on Mars. *J. Geophys. Res. E Planets* **120**, 1119–1140.

Cuif J. P., Dauphin Y. Y., Doucet J., Salome M. and Susini J. (2003) XANES mapping of organic sulfate in three scleractinian coral skeletons. *Geochim. Cosmochim. Acta* **67**, 75–83.

Dokken K. M., Parsons J. G., McClure J. and Gardea-Torresdey J. L. (2009) Synthesis and structural analysis of copper(II) cysteine complexes. *Inorganica Chim. Acta* **362**, 395–401.

Van Der Ent A., Callahan D. L., Noller B. N., Mesjasz-Przybylowicz J., Przybylowicz W. J., Barnabas A. and Harris H. H. (2017) Nickel biopathways in tropical nickel hyperaccumulating trees from Sabah (Malaysia). *Sci. Rep.* **7**.

Frierdich A. J. and Catalano J. G. (2012a) Controls on Fe(II)-activated trace element release from goethite and hematite. *Environ. Sci. Technol.* **46**, 1519–1526.

Frierdich A. J. and Catalano J. G. (2012b) Fe(II)-mediated reduction and repartitioning of structurally incorporated Cu, Co, and Mn in iron oxides. *Environ. Sci. Technol.* **46**, 11070–11077.

Frierdich A. J., Luo Y. and Catalano J. G. (2011) Trace element cycling through iron oxide minerals during redox-driven dynamic recrystallization. *Geology* **39**, 1083–1086.

Kelly R. A., Andrews J. C. and DeWitt J. G. (2002) An X-ray absorption spectroscopic investigation of the nature of the zinc complex accumulated in *Datura innoxia* plant tissue culture. *Microchem. J.* **71**, 231–245.

Luo Y., Giammar D. E., Huhmann B. L. and Catalano J. G. (2011) Speciation of selenium, arsenic, and zinc in Class C fly ash. *Energy Fuels* **25**, 2980–2987.

Manceau A. and Nagy K. L. (2012) Quantitative analysis of sulfur functional groups in natural organic matter by XANES spectroscopy. *Geochim. Cosmochim. Acta* **99**, 206–223.

Manceau A., Simionovici A., Lanson M., Perrin J., Tucoulou R., Bohic S., Fakra S. C., Marcus M. A., Bedell J. P. and Nagy K. L. (2013) *Thlaspi arvense* binds Cu(II) as a bis-(L-histidinato) complex on root cell walls in an urban ecosystem. *Metallomics* **5**, 1674–1684.

Montargès-Pelletier E., Chardot V., Echevarria G., Michot L. J., Bauer A. and Morel J. L. (2008) Identification of nickel chelators in three hyperaccumulating plants: An X-ray spectroscopic study. *Phytochemistry* **69**, 1695–1709.

Raj C. J., Joshi R. K. and Varma K. B. R. (2011) Synthesis from zinc oxalate, growth mechanism and optical properties of ZnO nano/micro structures. *Cryst. Res. Technol.* **46**, 1181–1188.

Schwertmann U. and Cornell R. M. (2000) *Iron Oxides in the Laboratory: Preparation and Synthesis*. VCH Publishers, New York.

Swanner E. D., Webb S. M. and Kappler A. (2019) Fate of cobalt and nickel in mackinawite during diagenetic pyrite formation. *Am. Mineral.* **104**, 917–928.